Spreading alpha-Synuclein Oligomers Trigger Astrocyte Reactivity and Astrocyte-glutamatergic Neuron system dysfunction in an Age-Dependent Manner

Jaehyun LeeBae[*2], Verena Bopp[*1], Alicia Goreth[2], Veselin Grozdanov[1], Julia K. Kühlwein[1], Ermanno Gazzola[2], Daniel Rombach[2], Laura Meier[1], Leda Dimou[1], Karin M. Danzer[1,2]

[1] Department of Neurology, University Clinic Ulm, 89081 Ulm, Germany
[2] German Center for Neurodegenerative Diseases (DZNE), 89081 Ulm, Germany
* These authors contributed equally

Figures: 7

Extended Data Figures: 8

Word count: 3349

Keywords: Parkinson's disease, transgenic mouse model, α-synuclein, spreading, spatial transcriptomics, single-nuclei RNA-sequencing, aging, visium spatial, astrocyte, glutamate

Correspondence:

Prof. Dr. Karin Danzer

DZNE Ulm

Albert-Einstein-Allee 11

89081 Ulm

Karin.danzer@dzne.de

Abstract

Parkinson's disease (PD) is characterized by the progressive accumulation and spatio-temporal spread of α-synuclein (α-syn) oligomers and a progressive loss of dopaminergic neurons. To investigate the transcriptional and cellular consequences of α-syn oligomer spreading, we employed spatial transcriptomics and single-nucleus RNA sequencing (snRNA-seq) in a transgenic PD mouse model. We identified α-syn spreading to the substantia nigra and defined a transcriptional "Spreading Signature" associated with α-syn pathology**.** We found an age specific increase in reactive astrocytes, close interactions between reactive astrocytes and α-syn, and transcriptional dysregulation of the astrocyte-glutamatergic neuron network. We further identified two subtypes of glutamatergic neurons that are vulnerable to astrocytic changes. Comparative analysis with human PD snRNA-seq data revealed conserved astrocytic dysfunctions, underscoring the translational relevance of our findings. Based on our results, we propose a revised model of α-syn spreading and highlight 36 genes as potential therapeutic targets for mitigating astrocyte-neuron dysfunction in PD.

Introduction

Parkinson's disease (PD), a chronic progressive neurodegenerative disease, is characterized pathologically by loss of dopaminergic neurons in the substantia nigra (SN) and the accumulation of aggregated α-synuclein (α-syn) in the form of Lewy bodies[1]. Based on observations by Heiko Braak et al., the α-syn pathology starts from the olfactory bulb and brainstem, and then spreads progressively to axonally connected areas throughout the CNS in a spatio-temporal manner, eventually reaching the SN[2]. Subsequent studies supported this theory as they reported the propagation of α-syn pathology from host to graft in PD patients[3-5] and the cell-to-cell spread of α-syn to anatomically connected regions in PD mouse models[6-9].

A substantial number of studies has demonstrated direct cytotoxic effects of pathologic α-syn on neurons, e.g. by pore-formation and calcium-influx, sequestering of the Na^+/K^+-ATPase, oxidative stress and mitochondrial damage[10-12]. However, other cell types can also be affected: microglia, astrocytes, oligodendrocytes and infiltrating immune cells show specific responses to extracellular α-syn and are believed to modulate the spread of pathology[13-15].

A powerful tool to investigate cellular changes by an extrinsic trigger is the study of transcriptomic changes, which can illuminate mechanistic insights and therapeutic targets in affected cells. Recent developments have enabled the resolution of transcriptomic changes to single-cells or spatial domains[16,17], which might help to elucidate the exact pathological cascade involving α-syn aggregation and transmission.

In a previous study, we established a transgenic PD human α-syn oligomer mouse model, showing neuronal cell-to-cell propagation of α-syn aggregates and α-syn pathology in SN, midbrain, and other regions[18]. To investigate the spatial and cell-type-

44 specific effects of α-syn oligomer spreading during aging *in-vivo*, we integrated single-
45 nucleus RNA sequencing (snRNA-seq) with spatial transcriptomics in this model,
46 enabling us to assess the direct consequences of α-syn oligomer propagation.

47 # Results

48 ## Defining a Spreading Area and "Spreading Signature"

49 To study the *in-vivo* spatial characteristics of α-syn spreading in PD, we utilized our
50 transgenic α-syn PD mouse model that recapitulates α-syn oligomer propagation and
51 accumulation at synapses within specific forebrain and midbrain regions, including the
52 SN[18].

53 Transcriptional changes in response to α-syn oligomer spreading were determined
54 using visium spatial transcriptomics on brain slices of 20-months (20M) and 3-months
55 (3M) old mice from the previously described PD mouse model, which is based on a
56 human α-syn protein complementation system expressing α-syn fused to non-
57 fluorescent Venus YFP halves (V1S and SV2). Fluorescent Venus YFP (V1S/SV2) is
58 reconstituted when α-syn oligomerization takes place (Figure 1 A). We included two
59 conditions: Double-transgenic mice expressing V1S/SV2 under the control of the tTA-
60 CaMKIIa transgene (ON) and single-transgenic mice lacking the tTA-CaMKIIa
61 transgene (OFF) as control (Figure 1 A). After filtering and clustering the integrated
62 data (Ext. Data Fig. 1) we identified spatially distinct cell clusters (Figure 1 B, Ext. Data
63 Fig. 2).

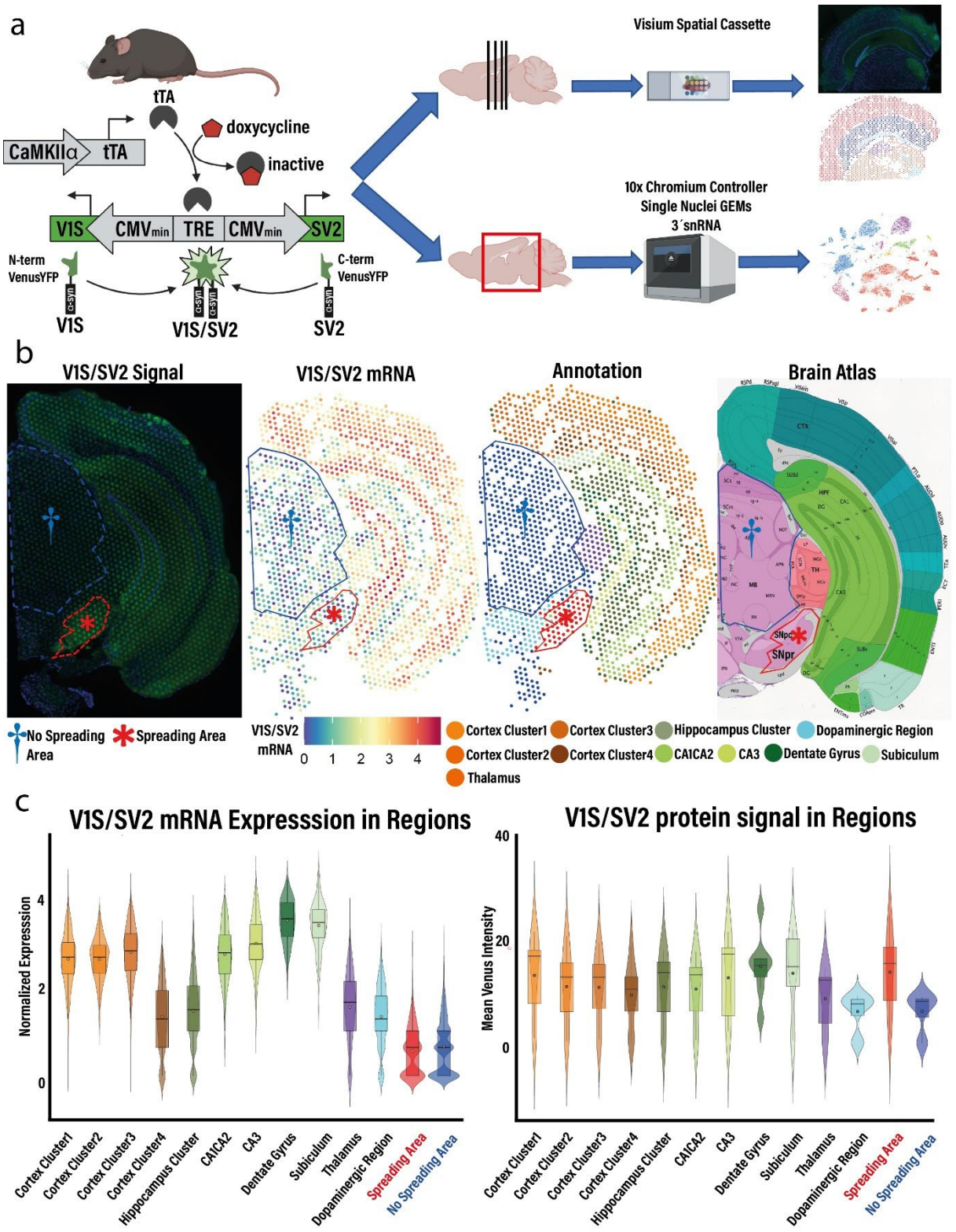

Figure 1. Spatial transcriptomics enables identification of a "Spreading Area" at the Substantia Nigra (SN) with spreading α-syn oligomers in an *in-vivo* PD mouse model

a, Schematic representation of the experimental design. Brain tissues from aged mice in a Venus-tagged human α-syn oligomer-based PD model was used to generate two datasets: Visium Spatial transcriptomics and snRNA. Both datasets included two conditions: ON (double-transgenic mice with

70 V1S/SV2 α-syn oligomer expression under the control of tTA-CaMKIIa transgene) and OFF (single-
71 transgenic mice without tTA-CaMKIIa). The Visium dataset comprised 3–4 brain slices per mouse, with
72 samples from three mice per condition, while the snRNA-seq dataset included samples from three mice
73 per condition. **b,** Brain slices in the Visium dataset were annotated using Louvain clustering, regional
74 markers obtained from mousebrain (mousebrain.org)[21] or published sources, and anatomical
75 information from the allen mouse brain atlas[19,20]. This approach enabled the assignment of anatomically
76 relevant cluster annotations. **c,** Among these, a specific subcortical region including the SN was
77 identified, which showed high V1S/SV2 protein expression (green Venus signal) but low V1S/SV2 mRNA
78 levels, suggesting V1S/SV2 spreading into this area. This region was defined as the "Spreading Area".
79 In contrast, a neighboring region with comparable V1S/SV2 mRNA levels but low Venus signal was
80 identified and designated as the "No Spreading Area".

81

82 We first focused on the 20M samples and annotated clusters to their respective
83 anatomical brain regions using the Allen mouse brain atlas[19,20] and regional marker
84 data (Suppl. Table 1) from mousebrain (mousebrain.org)[21] (Figure 1 B, Ext. Data Fig.
85 2). Notably, this approach identified one subcortical region with low V1S/SV2 mRNA
86 levels but high V1S/SV2 protein levels as indicated by elevated Venus fluorescence
87 signal, thus implying α-syn oligomer spreading to this region (named "Spreading
88 Area"). In contrast, another subcortical region exhibited comparable low V1S/SV2
89 mRNA expression but also low V1S/SV2 protein (named "No Spreading Area") (Figure
90 1 B, C).

91 This distinction provided a unique framework to investigate transcriptional changes
92 associated specifically with the spreading of α-syn oligomers. By comparing the
93 transcriptional profiles of the "Spreading Area" and "No Spreading Area" we aimed to
94 elucidate transcriptional and functional consequences of propagation of α-syn
95 oligomers.

96 For characterization of the “Spreading Area”, we defined a "Spreading Signature"
97 comprising two components: First, differentially expressed genes (DEGs) were
98 identified by comparing the "Spreading Area" and "No Spreading Area" regions (Suppl.
99 Table 2). Only DEGs that were significant in the ON condition but not in the OFF
100 condition were included (Ext. Data Fig. 3). Second, using the aforementioned DEGs,
101 transcription factors (TFs) that actively regulate these DEGs were inferred by using the
102 decoupleR[22] framework (Figure 2 A, Ext. Data Fig. 3 A). Together, these analyses
103 resulted in a transcriptional "Spreading Signature" encompassing a total of 135
104 genes/TFs (Figure 2 A, Suppl. Table 3).

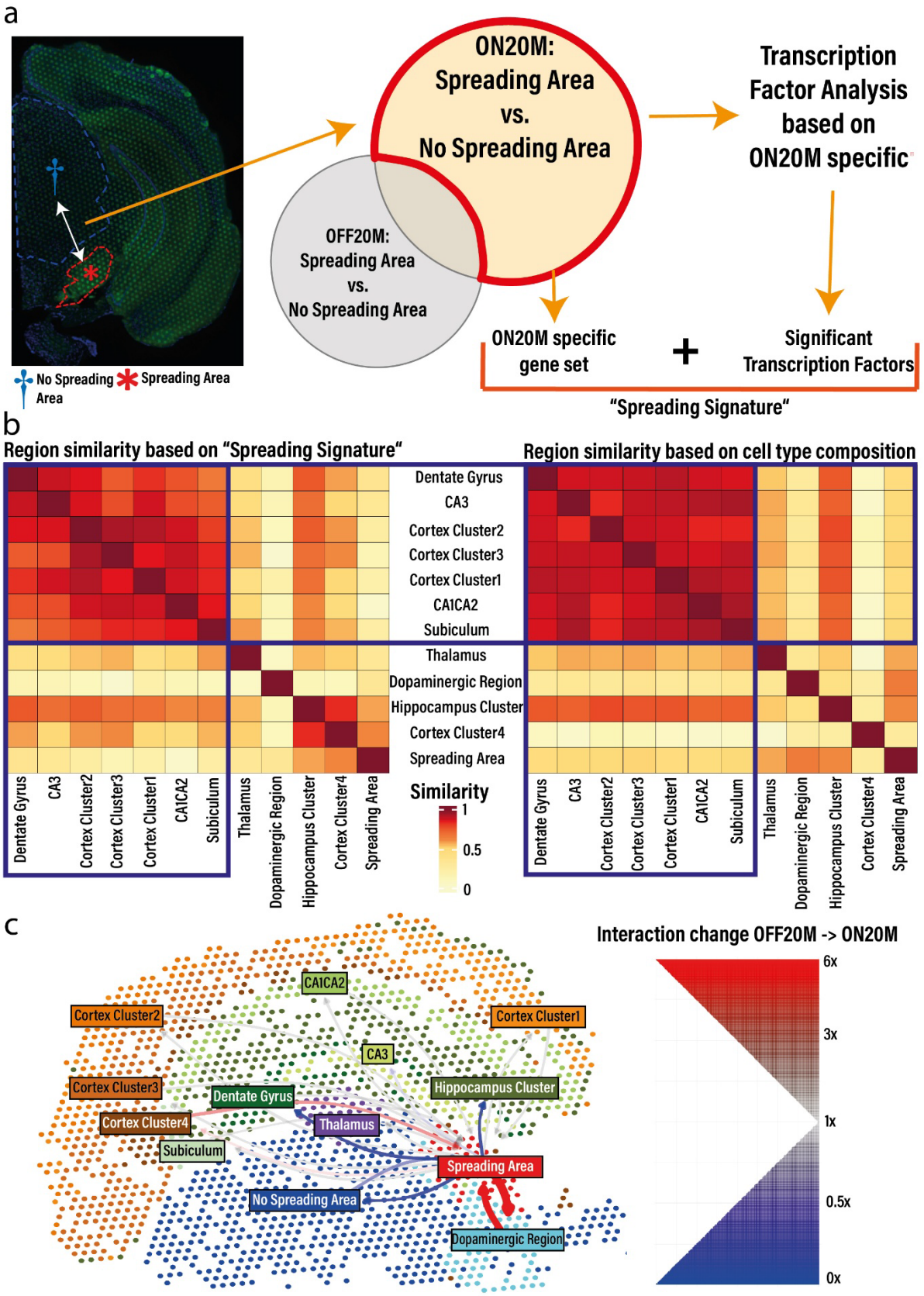

Figure 2. "Spreading Area" obtains α-syn oligomer spreading specific transcriptional profile and shows increased interactions with dopaminergic neuron enriched region

a, To investigate transcriptional changes associated with spreading, we conducted a differential gene expression analysis comparing the "Spreading Area" and "No Spreading Area" regions. We retained only DEGs that were unique to the ON condition ("ON-Spreading Area" vs. "ON-No Spreading Area"), subtracting those already identified in the OFF condition ("OFF-Spreading Area" vs. "OFF-No Spreading Area"). These ON-specific DEGs were subsequently analyzed for TF activity using the decoupleR[22] framework. Relevant TFs and the 20M ON-specific DEGs were consolidated to define the "Spreading Signature." **b,** Heatmaps depicting similarities among annotated Visium spatial regions are shown. The left heatmap illustrates region similarities based on Pearson correlation of the log2 fold changes of the "Spreading Signature". Notably, the "Spreading Signature" was absent in regions with native high expression of V1S/SV2 mRNA. This grouping pattern was mirrored in the right similarity heatmap, derived from the Aitchison similarity of the deconvoluted cell type compositions of the regions. This grouping pattern suggests that transcriptional differences between regions are partially explainable by variations in cell type composition. **c,** Changes in region-to-region LR interactions from OFF to ON conditions visualized on an exemplary sample. Notably, interactions between “Spreading Area” and "Dopaminergic Region" increased nearly six-fold.

To examine whether the “Spreading Signature” was unique to the “Spreading Area” we performed likeness analysis using the “Spreading Signature” between the annotated regions. We found that the “Spreading Signature” was mostly specific to the “Spreading Area” (Figure 2B). We hypothesized that these differences were primarily attributable to variations in cell type composition between regions, therefore we deconvoluted the visium spatial spots using snRNA-seq data from the same mouse model to compare cell type compositions between the regions. Indeed, the comparison indicated that the differences in DEGs of the "Spreading Area" from the cortical or hippocampal regions were largely explained by cell type composition differences (Figure 2 B, Ext. Data Fig. 3).

134 Additionally, ligand-receptor (LR) analysis revealed significant alterations in
135 interregional communications between different regions in response to V1S/SV2
136 oligomers mainly involving the "Spreading Area" (Suppl. Table 4). Notably, intercellular
137 communication between the “Spreading Area” and the tyrosine hydroxylase (TH)
138 enriched "Dopaminergic Region" increased nearly six-fold in 20M old mice when α-syn
139 oligomers are present, pointing to a strong impact of α-syn oligomers on the
140 interactions between dopaminergic neurons and the “Spreading Area” (Figure 2 C).

141 **α-syn spreading promotes astrocyte/neuron dysfunction**

142 To understand the biological and molecular meaning of the “Spreading Signature”, we
143 constructed a functional network with PIDC[23] using the “Spreading Signature” and
144 transcriptional data from the "Spreading Area" in 20M ON mice. We found that the
145 resulting functional network was composed of two subnetworks (Figure 3 A): The first
146 subnetwork was predominantly associated with astrocytic uptake and neurotransmitter
147 processing, including genes such as *Slc1a2*, an astrocyte-enriched
148 glutamate/excitatory amino acid transporter (EAAT) critical for glutamate clearance
149 and processing at synapses (Suppl. Table 3, Figure 3 A). The second subnetwork was
150 linked to astrocyte–neuron interaction dysfunctions, such as the astrocyte-neuron pre-
151 protein/neurotransmitter *Penk* (Suppl. Table 3). Together, functional network analysis
152 suggested a central role of astrocytes in α-syn spreading.

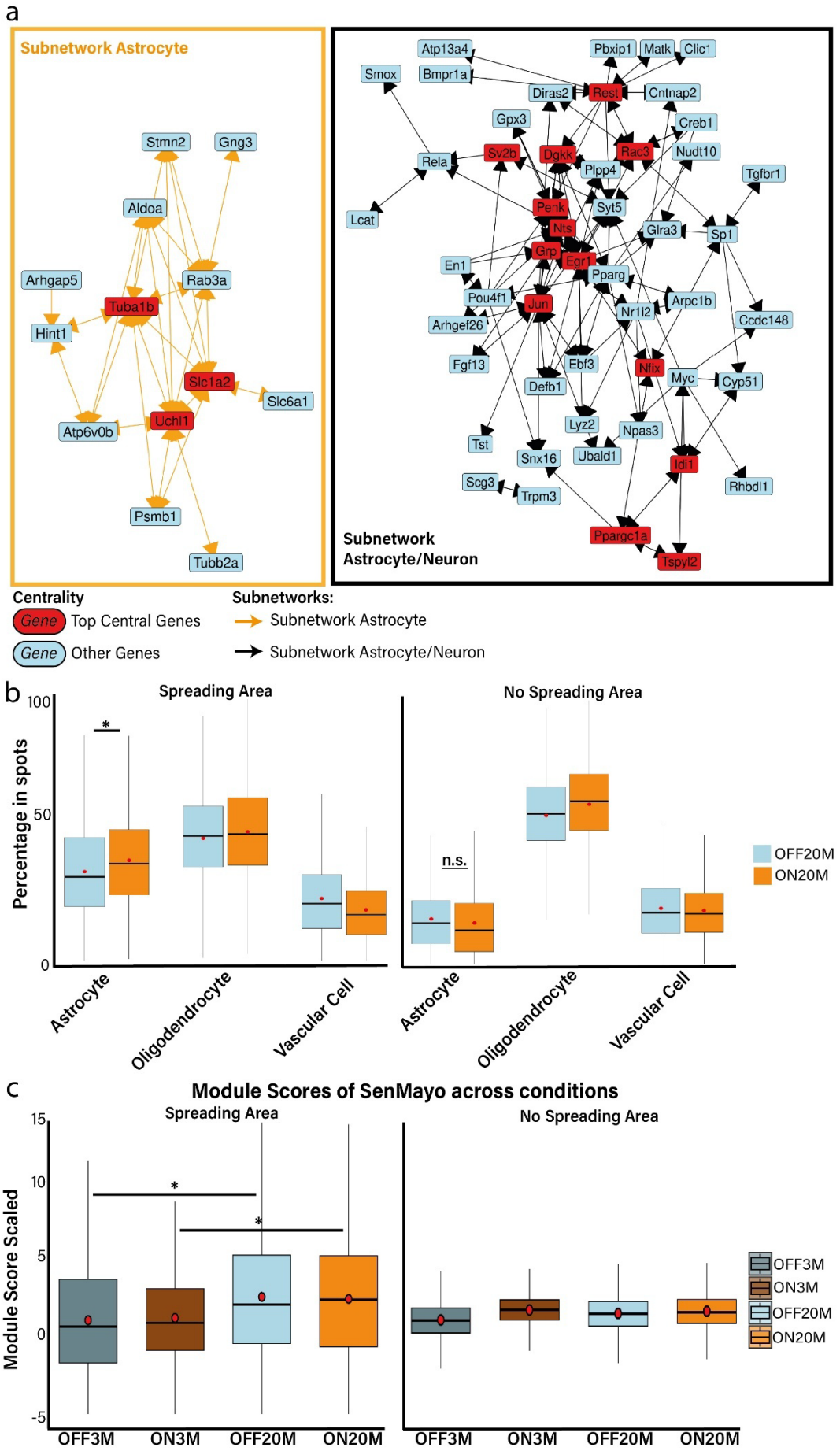
a
Subnetwork Astrocyte
Stmn2
Gng3
Aldoa
Arhgap5
Rab3a
Tuba1b
Hint1
Slc1a2
Slc6a1
Atp6v0b
Uchl1
Psmb1
Tubb2a
Atp13a4
Pbxip1
Matk
Clic1
Smox
Bmpr1a
Diras2
Rest
Cntnap2
Gpx3
Creb1
Rela
Sv2b
Dgkk
Rac3
Nudt10
Plpp4
Tgfbr1
Lcat
Penk
Syt5
Nts
Glra3
Sp1
Grp
Egr1
En1
Pparg
Pou4f1
Jun
Arpc1b
Nr1i2
Arhgef26
Ccdc148
Fgf13
Ebf3
Nfix
Myc
Cyp51
Defb1
Lyz2
Npas3
Tst
Snx16
Ubald1
Idi1
Scg3
Trpm3
Rhbdl1
Ppargc1a
Tspyl2
Subnetwork
Astrocyte/Neuron
Centrality
Gene Top Central Genes
Gene Other Genes
Subnetworks:
Subnetwork Astrocyte
Subnetwork Astrocyte/Neuron
b
Spreading Area
No Spreading Area
Percentage in spots
100
50
0
*
n.s.
OFF20M
ON20M
Astrocyte
Oligodendrocyte
Vascular Cell
c
Module Scores of SenMayo across conditions
Spreading Area
No Spreading Area
Module Score Scaled
15
10
5
0
-5
*
*
OFF3M
ON3M
OFF20M
ON20M

153

Figure 3. *In-silico* analysis of "Spreading Signature" and "Spreading Area" show central role of astrocytes in response to α-syn oligomer spreading.

a, A network was constructed using the "Spreading Signature," transcriptional data from the "Spreading Area", and known interactions from omniPath[67] and STRING[68] via the PIDC[23] algorithm. The network revealed two distinct subnetworks, with central genes identified based on betweenness centrality scores for both subnetworks. Functional annotations of the network genes, linked both subnetworks to astrocyte–neuron interactions, including astrocytic uptake and neurotransmitter glutamate processing (Suppl. Table 3). **b,** Significant changes in cell type composition between the OFF and ON conditions were assessed using tascCODA[70]. Shown here are the top three most represented cell types in the "Spreading Area". Astrocytes exhibited a significant (*: FDR < 0.2 in 60% of tascCODA iterations) increase in numbers in the "Spreading Area", whereas no significant changes were observed in the "No Spreading Area". **c,** Comparison of senescence levels across conditions and regions using the SenMayo[24] gene set. Scores are scaled to the mean of 3M OFF set to one. We only observed in the "Spreading Area" a significant (unpaired t-test, * FDR < 0.05) increase in senescence between the age groups. "No Spreading Area" showed no significant changes.

To further elucidate the central role of astrocytes, we investigated whether the astrocyte numbers were changed significantly in the "Spreading Area" between conditions. Indeed, based on transcriptomic data, we observed a significant increase of astrocyte numbers in the "Spreading Area" in response to α-syn oligomers (Figure 3 B). This increase in astrocyte numbers was not observed in the "No Spreading Area".

Furthermore, we also found senescence changes to differ between the "Spreading Area" and "No Spreading Area". We employed the SenMayo gene set[24] and studied possible changes of senescence in the "Spreading Area" between ages and α-syn oligomer presence. We observed a significantly higher enrichment of the SenMayo gene set in the "Spreading Area" during aging (Figure 3 C), while α-syn oligomer expression had no notable effect on senescence (Figure 3 C). The "No Spreading Area" showed no significant changes in the senescence during aging or as a response

182 to α-syn oligomer expression (Figure 3 C). This suggests that the “Spreading Area”
183 has a predisposition being vulnerable for age related changes compared to the “No
184 Spreading Area”. This might be responsible for the accumulation of spread α-syn
185 oligomers in the “Spreading Area” eventually leading to the observed transcriptional
186 changes in astrocytic function (Figure 3 A).

187 To further characterize interactions between astrocytes and α-syn oligomers in the SN
188 and to verify the increase of astrocyte numbers, we conducted immunohistochemical
189 (IHC) staining of 20M brain slices of our mouse model visualizing reactive astrocytes
190 using GFAP, α-syn oligomers by GFP, and dopaminergic neurons with TH (Figure 4,
191 Ext. Data Fig. 5). Manual counting indeed confirmed our *in-silico* findings and revealed
192 a significant increase in reactive astrocyte numbers in response to α-syn oligomers in
193 the SN of aged mice. Moreover, astrocytes displayed clear morphological changes
194 towards reactive hypertrophic astrocytes with thickened and elongated processes.
195 (Figure 4 A, B).

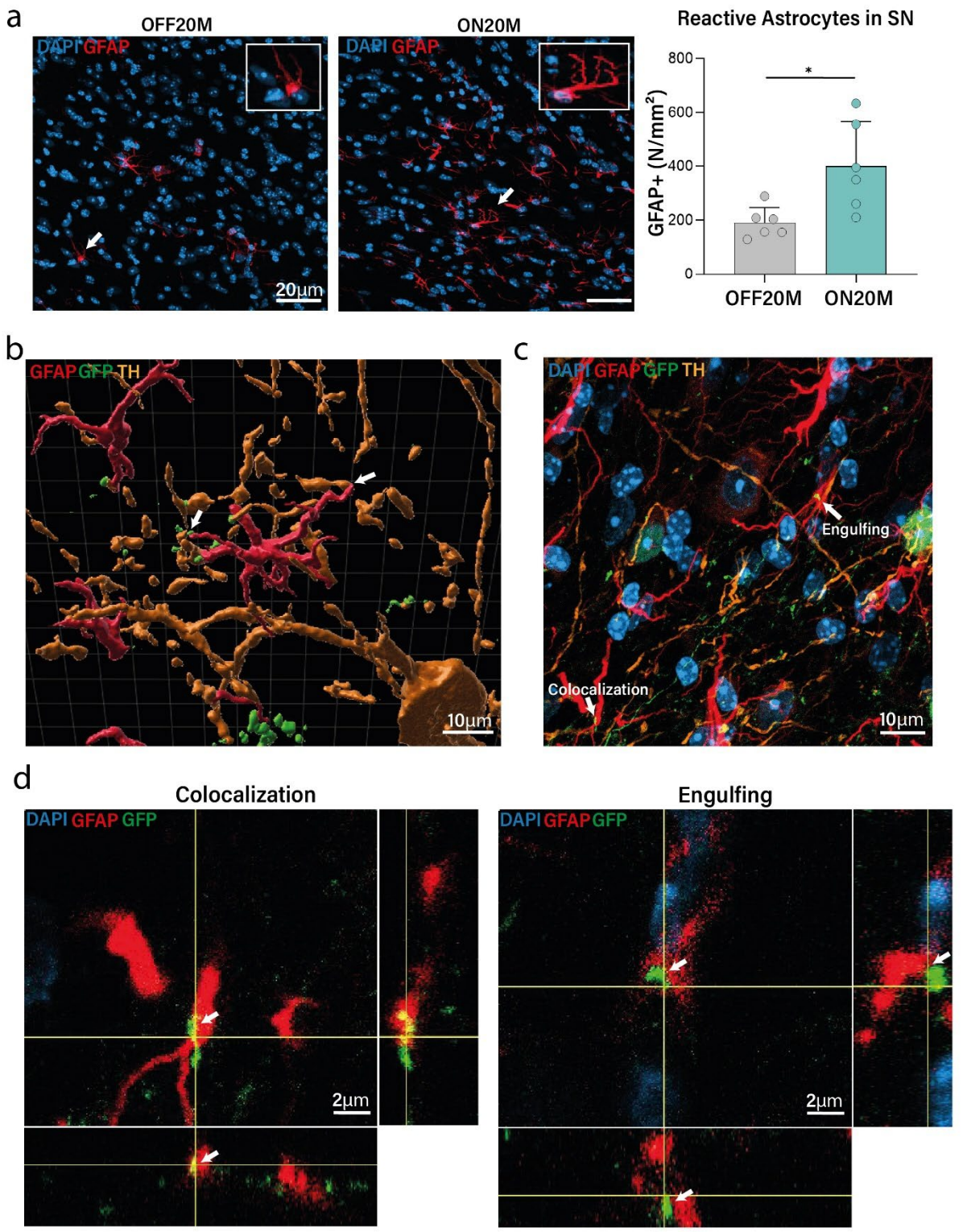

Figure 4. Expression of α-syn oligomers lead to increase in reactive astrocytes and uptake of α-syn oligomers by reactive astrocytes in the SN

a, Using brain slices from 20-months old mice from our PD model we performed IHC staining of reactive astrocytes (GFAP, red) and cell nuclei (DAPI, blue). Number of reactive astrocytes were manually counted. Microscopy images on the left show representative images of the OFF and ON conditions with

202 withe arrows highlighting reactive astrocytes included in the count. White boxes are zoomed in images
203 of the white arrow astrocytes. Quantification of reactive astrocytes in the SN revealed a significant
204 increase in their numbers in response to α-syn oligomer expression (n = 6; mean ± SD; unpaired t-test,
205 *p < 0.05, 40× magnification). **b,** Surface rendering of reactive astrocytes, V1S/SV2 α-syn oligomers
206 (GFP, green), and dopaminergic neurons (TH, orange) staining using the Imaris software on a
207 representative 20M ON brain slice. We observed contacts and close proximity between neurons,
208 reactive astrocytes and V1S/SV2. **c,** Z-stack maximum intensity projections of IHC staining in 20M ON
209 SN showed two distinct localization patterns of the V1S/SV2: (Engulfing) V1S/SV2 was found in close
210 proximity to reactive astrocytes being enclosed but not taken up by folding astrocytes and
211 (Colocalization) colocalized within reactive astrocytes. **d,** Magnified orthogonal projections of
212 "Colocalization" and "Engulfing" arrows in C. Bottom image: XZ-plane, right image: YZ-plane, middle
213 image: XY-plane. DAPI: Nucleus, GFAP: reactive astrocytes, GFP: V1S/SV2, TH: Dopaminergic neuron

214

215 Interestingly, we also found in the transcriptional data multiple central genes in the
216 "Spreading Signature" being related to reactive astrocytes such as e.g. *Egr1*, *Dgkk*,
217 *Rela, Ppargc1a, Tgfbr1, Bmpr1a* or *Hmgb3*. (Suppl. Table 3) further supporting the
218 involvement of reactive astrocytes.

219

220 Extracellular α-syn was mostly found at the end feet of reactive astrocytes and synaptic
221 ends (Figure 4 B). We further observed two distinct localization patterns of α-syn
222 oligomers in the context of reactive astrocytes: (1) Colocalization: α-syn taken up by
223 reactive astrocytes and (2) Engulfing: α-syn engulfed by astrocytes but not taken up
224 (Figure 4 C, D).

225 Taken together, using both transcriptional data as well as IHC data we could validate
226 *in-vivo* the increase of reactive astrocyte numbers and their close functional interaction
227 with α-syn oligomer spreading in the SN.

228 **Astrocytic dysfunction driven by α-syn spreading emerges only in aged mice**

229 To further specify the vulnerable cell types affected by α-syn spreading in the aged
230 mice we utilized snRNA-seq data of the same mouse model to calculate a Module
231 Score[25] for the "Spreading Signature" across all cell types and conditions in our
232 snRNA-seq dataset (Suppl. Table 6). Only the astrocytic subtypes - Astro-Slc1a2 and
233 Astro-Slc6a1 - exceeded the significance threshold (FDR < 0.05 & Effect size > 0.15;
234 Figure 5 A) again cementing the strong role of astrocytes in α-syn spreading found by
235 visium spatial data analysis. Notably, among the astrocyte subtypes the Astro-Slc1a2
236 subtype exhibited a much higher number of DEGs when comparing ON and OFF
237 condition (Ext. Data Fig. 7 E, Suppl. Table 6). This finding aligns with the central role
238 of *Slc1a2*, identified as a key gene in the "Spreading Signature" (Figure 3 A).

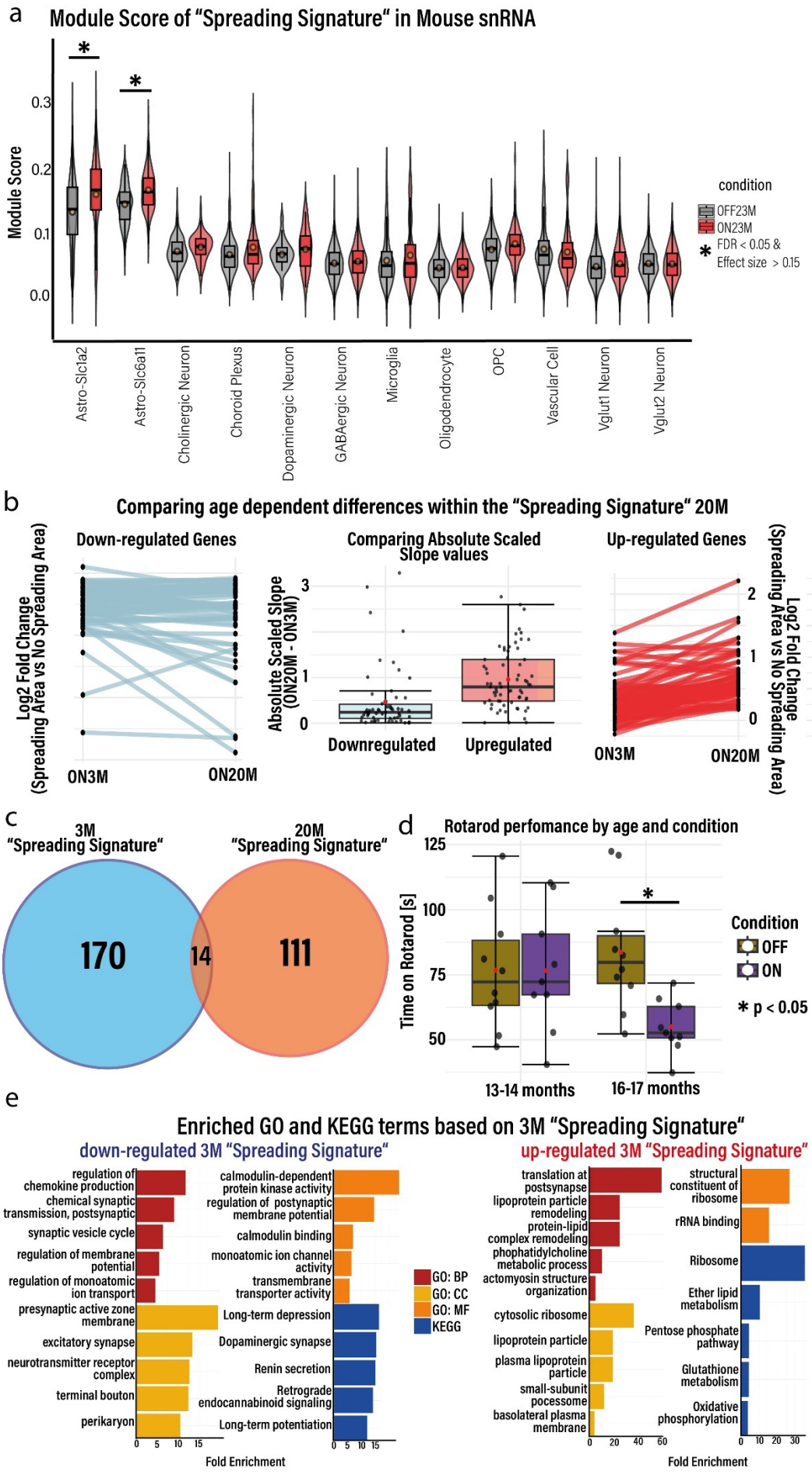
a
Module Score of "Spreading Signature" in Mouse snRNA
Module Score
0.0
0.1
0.2
0.3
*
*
condition
OFF23M
ON23M
* FDR < 0.05 & Effect size > 0.15
Astro-Slc1a2
Astro-Slc6a11
Cholinergic Neuron
Choroid Plexus
Dopaminergic Neuron
GABAergic Neuron
Microglia
Oligodendrocyte
OPC
Vascular Cell
Vglut1 Neuron
Vglut2 Neuron
b
Comparing age dependent differences within the "Spreading Signature" 20M
Down-regulated Genes
Log2 Fold Change (Spreading Area vs No Spreading Area)
ON3M
ON20M
Comparing Absolute Scaled Slope values
Absolute Scaled Slope (ON20M - ON3M)
0
1
3
Downregulated
Upregulated
Up-regulated Genes
Log2 Fold Change (Spreading Area vs No Spreading Area)
0
1
2
ON3M
ON20M
c
3M "Spreading Signature"
20M "Spreading Signature"
170
14
111
d
Rotarod perfomance by age and condition
Time on Rotarod [s]
125
100
75
50
*
13-14 months
16-17 months
Condition
OFF
ON
* p < 0.05
e
Enriched GO and KEGG terms based on 3M "Spreading Signature"
down-regulated 3M "Spreading Signature"
regulation of chemokine production
chemical synaptic transmission, postsynaptic
synaptic vesicle cycle
regulation of membrane potential
regulation of monoatomic ion transport
presynaptic active zone membrane
excitatory synapse
neurotransmitter receptor complex
terminal bouton
perikaryon
calmodulin-dependent protein kinase activity
regulation of postsynaptic membrane potential
calmodulin binding
monoatomic ion channel activity
transmembrane transporter activity
Long-term depression
Dopaminergic synapse
Renin secretion
Retrograde endocannabinoid signaling
Long-term potentiation
0 5 10 15
Fold Enrichment
GO: BP
GO: CC
GO: MF
KEGG
up-regulated 3M "Spreading Signature"
translation at postsynapse
lipoprotein particle remodeling
protein-lipid complex remodeling
phophatidylcholine metabolic process
actomyosin structure organization
cytosolic ribosome
lipoprotein particle
plasma lipoprotein particle
small-subunit pocessome
basolateral plasma membrane
structural constituent of ribosome
rRNA binding
Ribosome
Ether lipid metabolism
Pentose phosphate pathway
Glutathione metabolism
Oxidative phosphorylation
0 20 40 60
0 10 20 30
Fold Enrichment

239

240 **Figure 5. Motoric deficits and α-syn oligomer spreading related transcriptional changes of**
241 **astrocytes are age specific**
242 **a,** Using snRNA data from 23-months old mice of our PD mouse model we calculated a Module Score
243 of our "Spreading Signature" for all annotated cell types using the Seurat[25] function *AddModuleScore*.
244 Comparing the scores between the conditions, only the astrocytic subtypes cleared the significance
245 threshold of FDR < 0.05 and effect size > 0.15. **b,** We investigated our "Spreading Signature" of interest
246 at 20-months across the ages by comparing the log2 Fold Changes of the "Spreading Area" vs. "No
247 Spreading Area" comparison between 3M and 20M. While the down-regulated genes were similar in the
248 3M and 20M, we observed heightened up-regulation in the up-regulated genes. **c,** Comparing the α-syn
249 oligomer spreading specific "Spreading Signature" between 3 months and 20 months old mice showed
250 an age specific split in the "Spreading Signature". **d,** We checked for motoric deficits in our PD mouse
251 model by measuring time on the rotarod. Using 10 control (OFF) and 9 PD (ON) mice, their time on the
252 rotarod after training was measured between 13-14 months and 16-17 months of age. Only at the older
253 time point the ON mice showed a significant motoric deficit compared to the OFF mice. The statistical
254 testing was done by an unpaired student´s t-test with significance set at a p value lower than 0.05. **e,**
255 We checked the function of the 3M "Spreading Signature" by GO and KEGG term enrichment analysis.
256 For visualization enriched GO and KEGG terms (FDR < 0.05) were clustered by similarity and only
257 representative terms of the clusters were visualized. Down-regulated genes were linked to neuronal,
258 synaptic, and calcium signaling terms while up-regulated genes were enriched in ribosomal,
259 cytoskeleton, and mitochondrial functions

260

261 Next, we analyzed the "Spreading Area" also in younger mice and asked whether
262 related transcriptional changes also occur in young mice. Using the same methods as
263 for the 20M mice, we confirmed α-syn oligomer spreading in the same region in the 3M
264 spatial transcriptomics data (Ext. Data Fig. 6 C). Notably, the down-regulated genes
265 from the 20M "Spreading Signature" were similarly regulated in 3M and 20M. In
266 contrast to this, the up-regulated genes were highly elevated upon aging (Figure 5 B).
267 Moreover, Module Scores, stratified by up-regulated and down-regulated genes

268 showed that especially the up-regulated genes from the 20M old animals are enriched
269 in the astrocyte subtypes (Ext. Data Fig. 8 A). This suggests that aging is necessary
270 for astrocyte transcriptional changes to occur in response to α-syn oligomer spreading.

271 To get a more holistic transcriptional comparison between the age groups, we
272 determined the transcriptional characteristics of the 3M “Spreading Area” and defined
273 a "Spreading Signature" for the 3M old mice as for the 20M mice. There was only a
274 miniscule overlap between the 20M “Spreading Signature” and the 3M “Spreading
275 Signature” (Figure 5 C). Furthermore, we observed motoric disabilities for PD mice
276 only on the aged cohort (Figure 5 D) pointing to a connection between differing
277 transcriptional changes and the motoric deficits.

278 We further investigated the function of the 3M “Spreading Signature” and found genes
279 related to neuronal, synaptic, and calcium signaling function to be down-regulated,
280 while up-regulated genes were involved in ribosome, cytoskeleton, and mitochondrial
281 function (Figure 5 E).

282 Taken together, our findings suggest that the neuronal function has some disruptions
283 already at 3M that further progress during aging (Figure 5 E). During aging reactive
284 astrocytes get affected by α-syn oligomers (Figure 4; Figure 5 A, B; Ext. Data Fig. 8 A),
285 which may enhance the disruptive load on neuronal function, eventually leading to PD
286 phenotype (Figure 5 D).

287 **Dysregulations in the astrocyte-neuron glutamate system is recapitulated in PD**
288 **patients**

289 To investigate whether the observed astrocytic changes extend to neuronal changes
290 we used our snRNA-seq data from 23-months old mice and performed Gene Ontology
291 (GO) and KEGG pathway enrichment analyses of the Astro-Slc1a2 DEGs. Since the

292 PD motoric phenotype was only observed in the aged mice groups we focused on the
293 aged mice for further analysis.

294 GO and KEGG pathway analysis highlighted glutamatergic synapses**,** neurotransmitter
295 cycles and TCA-cycle metabolism (Figure 6 A, Suppl. Table 3). Furthermore, using the
296 same methodology as for the network inference from the 20M "Spreading Signature",
297 we constructed a functional network for the Astro-Slc1a2 DEGs from the snRNA-seq
298 data (Ext. Data Fig. 8 B) and found *Grm5* as a prominent central gene which
299 corresponds to the metabotropic glutamatergic receptor 5 (mGluR5) on a protein level.
300 Interestingly, mGluR5 plays an essential role in glutamate signaling and astrocyte-
301 neuron interactions[26-28] (Suppl. Table 3).

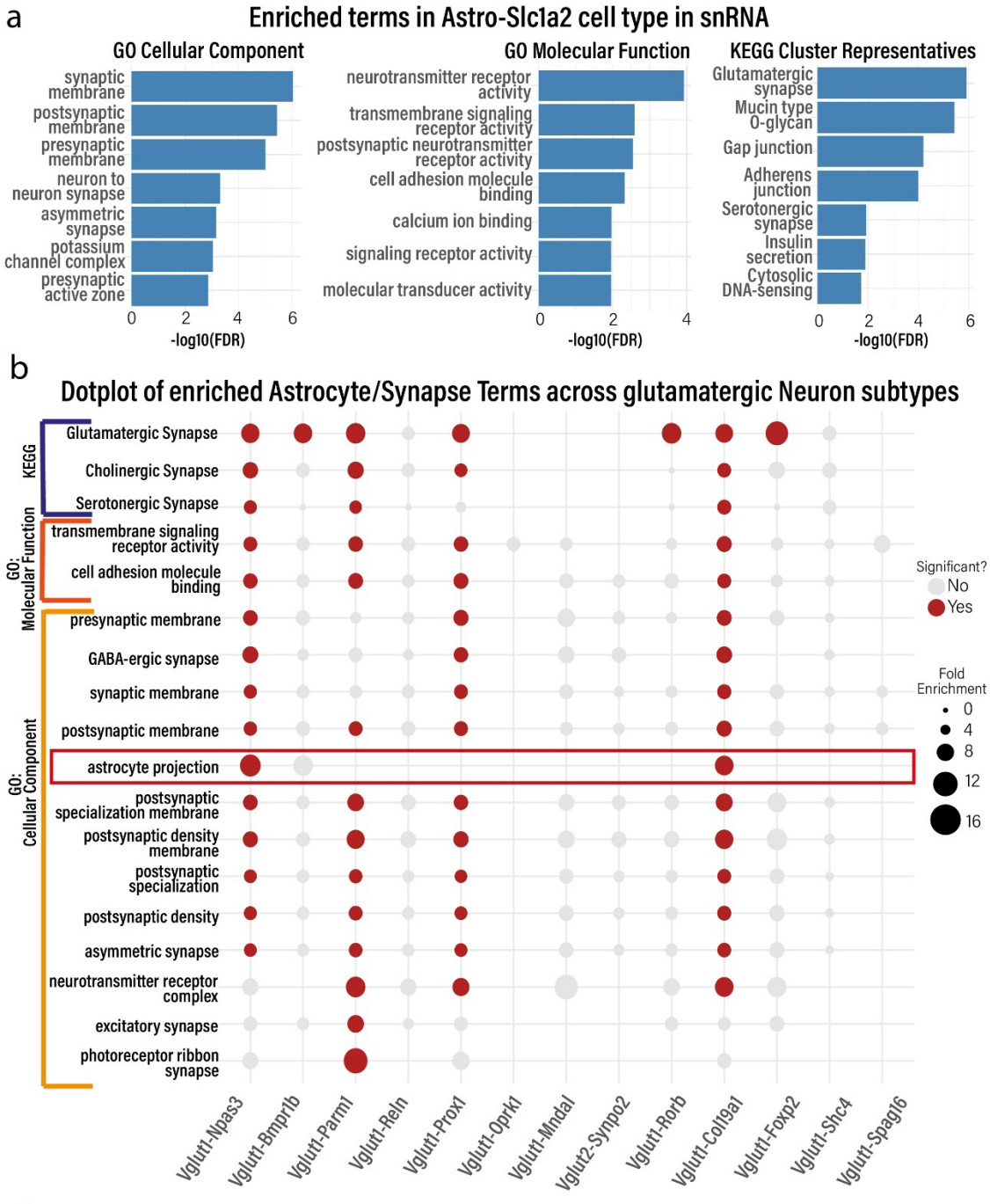
a
Enriched terms in Astro-Slc1a2 cell type in snRNA
GO Cellular Component
synaptic membrane
postsynaptic membrane
presynaptic membrane
neuron to neuron synapse
asymmetric synapse
potassium channel complex
presynaptic active zone
-log10(FDR)
GO Molecular Function
neurotransmitter receptor activity
transmembrane signaling receptor activity
postsynaptic neurotransmitter receptor activity
cell adhesion molecule binding
calcium ion binding
signaling receptor activity
molecular transducer activity
-log10(FDR)
KEGG Cluster Representatives
Glutamatergic synapse
Mucin type O-glycan
Gap junction
Adherens junction
Serotonergic synapse
Insulin secretion
Cytosolic DNA-sensing
-log10(FDR)
b
Dotplot of enriched Astrocyte/Synapse Terms across glutamatergic Neuron subtypes
KEGG
GO: Molecular Function
GO: Cellular Component
Glutamatergic Synapse
Cholinergic Synapse
Serotonergic Synapse
transmembrane signaling receptor activity
cell adhesion molecule binding
presynaptic membrane
GABA-ergic synapse
synaptic membrane
postsynaptic membrane
astrocyte projection
postsynaptic specialization membrane
postsynaptic density membrane
postsynaptic specialization
postsynaptic density
asymmetric synapse
neurotransmitter receptor complex
excitatory synapse
photoreceptor ribbon synapse
Vglut1-Npas3
Vglut1-Bmpr1b
Vglut1-Parm1
Vglut1-Reln
Vglut1-Prox1
Vglut1-Oprk1
Vglut1-Mndal
Vglut2-Synpo2
Vglut1-Rorb
Vglut1-Col19a1
Vglut1-Foxp2
Vglut1-Shc4
Vglut1-Spag16
Significant?
No
Yes
Fold Enrichment
0
4
8
12
16
c
Comparison of astrocytes between PD mice model and human PD patient snRNA data
Log2 FoldChange Mouse Slc1a2 Astrocyte
Log2 FoldChange Human Astrocyte
GRM5
SRCIN1
ROBO1
PLP1
CNTNAP2
Concordant Genes
Disconcordant Genes

302

303 **Figure 6. Single nucleus RNA data indicates α-syn oligomer related disruptions in the Astrocyte-**
304 **glutamatergic neuron system (Astro-GluN) in specific glutamatergic neuron subtypes and in**
305 **both mouse and human astrocytes**
306 **a,** Enriched Gene Ontology (GO) and KEGG terms of the Astro-Slc1a2 DEGs showed terms related to
307 glutamatergic synapses, neurotransmitter cycles and Astro-GluN system. **b,** GO and KEGG pathway
308 enrichment analyses were performed on DEGs from each glutamatergic subtype. We filtered for
309 significant terms (padj < 0.05) and visualized particularly terms related to "synapse" or "astrocyte“ (s.
310 Methods: *Term Enrichment analysis*). Notably, only the Vglut1-Npas3 and Vglut1-Col19a1 subtypes
311 included "astrocyte projection" among its significant terms, highlighting a unique link between these
312 subtypes and astrocytic processes. **c,** Comparison of log2 foldchanges of Astro-Slc1a2 DEGs between
313 mouse and human snRNA datasets. We used the Smajic et al. snRNA dataset that included astrocytes
314 from the SN of six PD patients and six sex-age matched controls. The labelled genes are the top 5 most
315 central genes of the Astro-Slc1a2 DEG network. While all DEGs show moderate concordance, the
316 central genes related to Astro-GluN system display strong concordance between mouse and human
317 snRNA data.
318

319 Together, we found *Grm5* – essential for glutamate signaling – as a central gene in the
320 vulnerable *Slc1a2* enriched astrocyte subtype, indicating dysfunctions in the astrocyte-
321 glutamatergic neurons (Astro-GluN) interactions in response to α-syn oligomers.

322 Since we were capable to show transcriptional changes in astrocytes related to Astro-
323 GluN interactions via multiple modalities, we next focused on glutamatergic neurons.
324 We used our snRNA-seq dataset and annotated 13 distinct glutamatergic neuron
325 subtypes to study enriched GO and KEGG terms for each glutamatergic subtype (Ext.
326 Data Fig. 7 C). Although the analysis was based on DEGs between conditions in
327 glutamatergic neuron subtypes, we obtained the term “astrocyte projection” as a
328 significantly enriched term in the subtypes Vglut1-Npas3 and Vglut1-Col19a1 (Figure
329 6 B). Both cell types also significantly downregulated *Grm3*, a gene transcribing the
330 metabotropic glutamate receptor 3 (mGluR3). This aligned with our previous

331 observations since astrocytes already pointed to mGluR5 to be central in α-syn
332 oligomer related changes. These findings suggest that those two subtypes have an
333 increased vulnerability to astrocytic changes and potentially to the aforementioned
334 dysfunctions in the Astro-GluN system, with mGluRs possibly playing a pivotal role in
335 the transmission of pathology between astrocytes and neurons.

336 Based on our *in-vivo* analysis of spatial data, snRNA-seq data, and confocal imaging
337 from our PD mouse model, we could pinpoint the effects of α-syn oligomer spreading
338 to reactive astrocytes and changes in the Astro-GluN system in two distinct
339 glutamatergic subtypes. Next, we compared our findings to human data and found
340 comparable transcriptional changes between our snRNA-seq mouse data and human
341 PD data related to Astro-GluN interactions.

342 We employed the PD snRNA-seq dataset from Smajic et al.[16], which includes major
343 glial cell types from the SN of PD patients and age-/sex-matched controls and
344 compared the log2 fold changes of Astro-Slc1a2 DEGs between mouse Astro-Slc1a2
345 cells to human astrocyte cells.

346 While the DEGs exhibited moderate concordance overall, the central genes from our
347 snRNA-seq mouse network (Ext. Data Fig. 8 B) -particularly those involved in Astro-
348 GluN system- displayed strong concordance between mouse and human data (Figure
349 6 C).

350 As genes from the Astro-GluN system, including the aforementioned *Grm5*, show solid
351 concordance between mouse and human astrocyte data, we suggest that the
352 diminished function of the Astro-GluN system through transcriptional changes, is also
353 present in human PD patients. This supports the translational importance of astrocytes
354 and the Astro-GluN system in PD pathology.

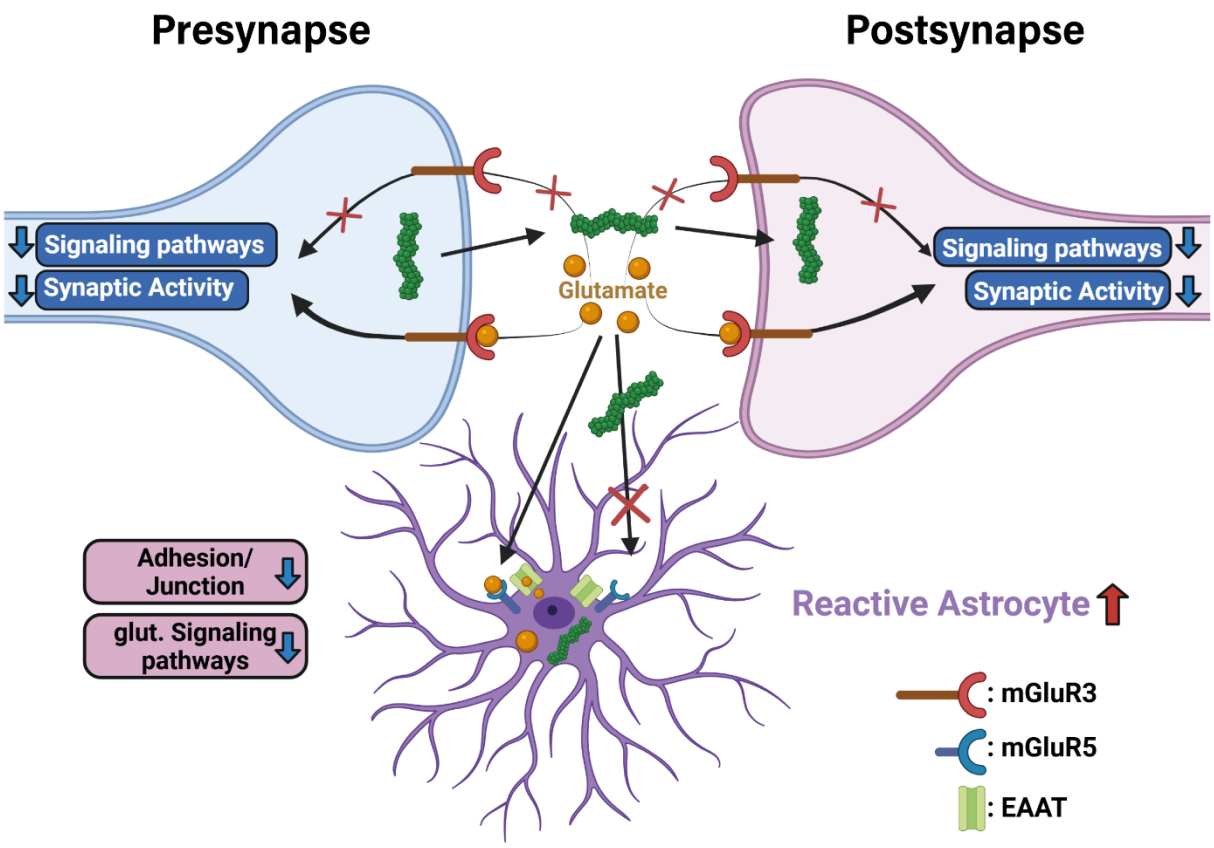

Figure 7. Revised model of α-syn oligomer spreading including the Astrocyte-GluN system dysfunctions

Proposed model for PD pathology associated with α-syn oligomer spreading. We hypothesize that the accumulation of α-syn oligomers at the synaptic cleft arises from both neuronal spreading and impaired astrocytic degradation of α-syn oligomers. This impairment may stem from diminished signaling pathways and cell-cell junctions in astrocytes. The accumulation of α-syn oligomers leads to an increase of reactive astrocyte numbers. The main damage of astrocytic impairment seems to be the astrocyte-neuron glutamate system, in which the synaptic accumulation of α-syn oligomers disrupts glutamatergic recycling and signaling in both astrocytes and glutamatergic neurons/synapses. Especially the genes *Slc1a2* (EAAT: Glutamate channel) and the mGluR genes *Grm3* and *Grm5* (mGluR3/mGluR5) are major players in this pathology. With less signaling occurring at the synapses, the affected synapses will start to degrade and lead to known PD effects. In summary, the spread of α-syn oligomers drives synaptic dysfunction and degeneration, alongside the activation of astrocytes, culminating in the progression of PD pathology.

372 ## Discussion

373 Based on multiple modalities this study demonstrates transcriptional and physiological
374 changes of the SN *in-vivo* in response to α-syn oligomer spreading. We confirmed
375 activation of astrocytes, transcriptional changes in astrocytes related to the Astro-GluN
376 system, and vulnerable subtypes of glutamatergic neurons. Notably, we observed that
377 astrocyte changes only occur in aged mice and provide evidence that these changes
378 might be linked to motoric phenotypes. Based on our findings, we propose a model of
379 α-syn oligomer spreading involving reactive astrocytes, glutamatergic synapses, and
380 a damaged Astro-GluN system (Figure 7) and report 36 genes centrally involved in this
381 model of α-syn oligomer spreading (Suppl. Table 3).

382 Multiple studies consistently reported the importance of astrocytes in PD and their
383 interactions with α-syn[29-35]. Moreover, Loria et al.[32] were able to demonstrate a role for
384 astrocytes in degradation of pathological α-syn fibrils in co-cultures of primary neurons
385 and astrocytes. In line with this, EVs derived from erythrocytes and containing α-syn
386 oligomers were shown to accumulate in astrocyte endfeet impairing glutamate uptake
387 likely via EAAT channel when injected into mice[36].

388 Extending on previous findings, we show *in-vivo* that in response to α-syn oligomer
389 spreading, astrocytes become reactive, increase in numbers, and change their
390 transcriptional profile in the SN. We report a gene program in the SN specifically
391 affected by α-syn oligomer spreading. This molecular architecture could confirm the
392 previously reported astrocytic changes involving *Slc1a2*/EAAT and introduce new
393 central genes in the α-syn oligomer spreading specific transcriptional profile changes.

394 Furthermore, previous studies already reported the ability of α-syn oligomers to affect
395 astrocytic functions in recycling glutamate[31,37,38], such as Trudler et al.[38] showing that

396 α-syn oligomers induced astrocytes to release more glutamate and thereby increase
397 glutamatergic signaling in human primary neurons from induced pluripotent stem cells.
398 Our data are in line with these prior findings, moreover, we report the underlying
399 transcriptional changes including downregulation of genes related to glutamate
400 receptors, astrocytic junctions, and glutamatergic signaling in both astrocytes and in
401 vulnerable glutamatergic neurons. This might offer specific central targets to rescue
402 the Astro-GluN system. Indeed, we point to mGluRs to play a major role in the transition
403 of damage from astrocytes to GluNs and in the overall disruption of the Astro-GluN
404 system, as we found mGluRs (*Grm3* and *Grm5*) as central players in either the affected
405 astrocytes or the more vulnerable glutamatergic neuron subtypes. Importantly,
406 mGluR3 and mGluR5 have already been shown to be of importance in human
407 astrocytes for the Astro-GluN system[39].

408 Previously, mGluRs have been implicated in PD multiple times[40-42] with for example
409 mGluR5 antagonists being protective of dopaminergic neurons in PD animal
410 models[43,44]. We align mGluRs into α-syn oligomer spreading related Astro-GluN
411 dysfunctions and suggest that the disruptions in mGluR signaling, diminished recycling
412 of glutamate via astrocyte, and blockades due to accumulation of α-syn oligomers in
413 astrocytes, neurons, and extracellular space, lead to diminished glutamatergic
414 signaling between the synapses. Following the synapse formation/elimination rules[45],
415 the synapses and neurons with less signaling activity devolve and are eliminated.

416 We further suggest that the involvement of reactive astrocytes in our model only occur
417 with sufficient aging and that this involvement is necessary for PD phenotypes to
418 emerge. We observed higher vulnerability to age related effects in our "Spreading
419 Area" by enrichment of the SenMayo gene set pointing to senescence. Whether and
420 how senescence-driven mechanisms contribute to α-syn accumulation and Astro-GluN

421 dysfunctions has to be determined in future studies. It might be that senescent glial
422 cells may facilitate the cell-to-cell spread of pathological proteins and senescence is
423 surely well established as a factor in aging[46] and age related neurodegenerative
424 diseases like PD or Alzheimer´s Disease[47,48]. Of note, α-syn aggregates have been
425 shown to spread in patterns correlating with regional senescence markers in PD[49].
426 Thus, our data further emphasizes reactive astrocytes as an age dependent player in
427 the development of PD phenotypes through α-syn oligomer spreading. Our findings
428 are supported by previous studies that showed reactive astrocyte/astrocytic
429 vulnerabilities are highly correlated with aging in mouse and human brains[50-52].

430 Here we report a unique gene set found to be central players in the transcriptional
431 changes of astrocytes and vulnerable GluN subtypes in response to α-syn oligomer
432 spreading. These include down-regulated genes related to glutamatergic signaling,
433 astrocyte-neuron junctions, and protein transport system and increased expression of
434 genes involved in activation of astrocytes, phagocytosis, synapse elimination, and
435 elevated oxidative stress.

436 In summary, we show the importance of the Astro-GluN system dysfunction in the
437 context of spreading of α-syn oligomers *in-vivo* and suggest that these 36 central
438 genes as a potential therapeutic target to combat PD related Astro-GluN dysfunction.
439

440 # Methods

441 *Generation and Housing of Transgenic Animals*

442 The transgenic mouse model B6.Cg-Tg(CamK2a-tTA)Mmay/DboJ x B6-Tg(ind alphα-
443 syn split Venus)D1 GVO was established in collaboration with Dr. Björn von Einem
444 from the Department of Neurology and Olena Sakk from the Core Facility for
445 Transgenic Animals. The process was conducted with guidance of Dr. Bernd Baumann
446 from the Institute of Physiological Chemistry at Ulm University. Detailed phenotypic
447 characterization of these transgenic mice has been previously published[18].

448 The animals were maintained under standardized environmental conditions at the
449 Animal Research Center of Ulm University. The mice used in this study were double-
450 transgenic for V1S/SV2 and calcium/calmodulin-dependent protein kinase II alpha
451 (CamKIIa)[53], with transgene expression being regulated by doxycycline in a Tet-off
452 system[18]. To suppress transgene expression, 100 mg/ml doxycycline was administered
453 via the drinking water, which was supplemented with 10 g/l glucose to improve
454 palatability. For mice in which transgene expression was to be activated, drinking water
455 contained only glucose (10 g/l) without doxycycline.

456 The animals were housed in groups within open polycarbonate type II long cages.
457 Environmental parameters were stringently controlled, including temperature, humidity
458 and a 12-hour light/dark cycle. Food and water were provided *ad libitum* to ensure
459 unrestricted access. To promote animal welfare, the cages were enriched with nesting
460 material and polycarbonate shelters.

461 The V1S/SV2 mouse model employs a bioluminescent protein complementation assay
462 that facilitates the detection of α-syn aggregation. This system involves the expression
463 of human wild-type α-syn fused to either the N-terminal or C-terminal fragment of

464 yellow fluorescent protein (YFP), referred to as V1S and SV2, respectively. The
465 simultaneous expression of these two fragments enables their reconstitution into a
466 functional fluorescent protein upon aggregation of α-syn.

467 *Rotarod experiments*

468 All mice performed accelerating rotarod (Panlab Harvard LE8205) at the same days in
469 the same order. The experiment was adjusted to increase from 4 to 40 rpm over a
470 period of 300 s and was carried out in three consecutive trials with 5 min break in
471 between. The latency to fall was recorded and mean values were used for analysis.

472 *Nuclei Isolation*

473 To isolate nuclei from murine brain tissue, approximately 100 mg of brain material was
474 dissected from a single hemisphere, spanning the region from 0 to -5 mm relative to
475 Bregma, using a mouse coronal brain matrix (Cell Point Scientific). Brain tissue from
476 two animals was pooled to ensure sufficient material for subsequent isolation
477 procedures. All experimental steps were carried out on ice to maintain sample integrity.

478 Initially, 1,400 µl of homogenization buffer (320 mM Sucrose, 5 mM $CaCl_2$, 3 mM
479 $Mg(Ac)_2$, 10 mM Tris HCl pH 8, 0.1 mM EDTA pH 8, 0.1 % Nonidet P40 Substituent
480 (NP-40), 1 mM β-mercaptoethanol, 0.4 U/µl RiboLock in H_2O) was added to a douncer
481 containing the dissected brain tissue. The tissue was mechanically homogenized using
482 pestle A, followed by further homogenization with pestle B. The resulting homogenate
483 was filtered sequentially through 70 µm and 40 µm Flowmi cell strainers to eliminate
484 debris and large particles.

485 Subsequently, 700 µl of the filtered homogenate was combined with 450 µl of a working
486 solution (50 % Opti-Prep, 5 mM $CaCl_2$, 3 mM $Mg(Ac)_2$, 10 mM Tris HCl pH 8, 0.1 mM
487 EDTA, 1 mM β-mercaptoethanol in H_2O). A density gradient was prepared using 300
488 µl of 40 % Opti-Prep (with 96 mM Sucrose, 5 mM $CaCl_2$, 3 mM $Mg(Ac)_2$, 10 mM Tris

489 HCl pH 8, 0.1 mM EDTA, 0.03 % NP-40, 0.12 U/µl RiboLock in H_2O), 750 µl of 30 %
490 Opti-Prep (with 134 mM Sucrose, 5 mM $CaCl_2$, 3 mM $Mg(Ac)_2$, 10 mM Tris HCl pH 8,
491 0.1 mM EDTA pH 8, 1 mM β-mercaptoethanol, 0.04 % NP-40, 0.17 U/µl RiboLock in
492 H_2O) and 700 µl of the homogenized tissue mixture. The density gradient was
493 centrifuged at 10,000 g for 5 min at 4 °C.

494 Following centrifugation, 200 µl of the isolated nuclei were carefully aspirated and
495 transferred into a 1.5 ml low-DNA-binding tube. To preserve nuclear integrity, 250 µl of
496 a solution containing 2 % BSA and 0.12 U/µl RiboLock in PBS was added. The mixture
497 was centrifuged at 2,000 g for 3 min at 4 °C, and the supernatant was discarded. The
498 resulting pellet was resuspended in 250 µl of the same 2 % BSA/RiboLock solution
499 and subjected to a second round of centrifugation under identical conditions. The
500 supernatant was discarded, and the pellet was resuspended in 250 µl of 2 %
501 BSA/RiboLock solution. The suspension was filtered through a 40 µm Flowmi cell
502 strainer into a fresh low-DNA binding tube. A final centrifugation at 2,000 g for 3 min at
503 4 °C was performed to pellet the nuclei.

504 The resulting pellet was resuspended in 50 µl of 1x nuclei buffer, prepared by diluting
505 10X Genomics nuclei buffer with the addition of 1 mM dithiothreitol (DTT) and 1 U/µl
506 RiboLock in H_2O. To evaluate the integrity and quantity of the isolated nuclei, a DAPI
507 stain was applied to visualize nuclear membrane integrity. The isolated nuclei were
508 subsequently used for snRNA-seq experiments. This was done for three mice per
509 condition.

510 *Single-nuclei RNA Sequencing*

511 The “Chromium 3’ Single Cell Gene Expression and Library Kit” (10x Genomics) was
512 used to generate the Gel Beads-In-Emulsion (GEMs), following the guidelines provided
513 by the manufacturer. Shortly, 22,000 of the isolated nuclei from mouse brain tissue

514 were introduced into barcoded Gel Beads using the Chromium Controller. Following
515 GEM-RT incubation, cDNA samples underwent recovery, purification and amplification
516 through a cDNA amplification reaction. Quality assessments on the amplified cDNA
517 were conducted using a High Sensitivity DNA Kit (Agilent) on a TapeStation platform.
518 Libraries were subsequently generated through the processes of fragmentation and
519 adaptor ligation. Sample Index PCR was executed and the resulting purified libraries
520 underwent assessment on TapeStation using a High Sensitivity DNA Kit to evaluate
521 fragment quality. The single-nucleus libraries were then sent to Novogene (United
522 Kingdom) for sequencing with the NovaSeq 6000.

523 *Visium spatial brain slice preparation*

524 To prepare tissue samples for visium spatial gene expression experiments, fresh-
525 frozen tissue specimens were utilized. The animals were euthanized using fast cervical
526 dislocation and the brain was immediately dissected. A metal beaker was filled with
527 isopentane and placed into a liquid nitrogen dewar to allow for rapid cooling. Sufficient
528 contact between the isopentane and the liquid nitrogen was ensured. The fresh tissue
529 sample was positioned in a cryomold and coated with TissueTek embedding medium.
530 The cryomold containing the embedded tissue was lowered into the chilled isopentane
531 and held in place until the TissueTek medium had fully solidified. Once the tissue was
532 completely frozen, it was transferred to dry ice and afterwards stored in a sealed
533 container at -80 °C for long-term preservation.

534 For sectioning, the cryostat was set to -20 °C. The frozen tissue block was removed
535 from storage and allowed to equilibrate briefly at cryostat temperature. The tissue block
536 was sectioned into slices with a thickness of 10-12 µm using the cryostat. Each section
537 was carefully transferred onto a visium gene expression slide by gently touching the
538 section to the active surface of the slide. After mounting the tissue section, the slide

539 was immediately placed into a storage container at -80 °C. The slides were maintained
540 at this temperature until further processing to preserve RNA integrity and spatial
541 organization. This was done for three mice per condition and we included 3-4 brain
542 slices per mice.

543 *Visium spatial immunofluorescence staining*

544 Prior to the visium spatial gene expression protocol, the sections were incubated for 1
545 min at 37 °C and subsequently fixed in cold methanol for 30 min at -20 °C. All following
546 steps were carried out in the visium slide cassette. The sections were then stained with
547 a fluorescent anti-GFP antibody to visualize the V1S/SV2 aggregates. A total of 70 µl
548 of 1x Blocking Buffer (3x SSC Buffer, 2 % BSA, 0.1 % Triton X-100 (w/v), 1 U/µl RNase
549 inhibitor, 10 % Ribonucleoside Vanadyl Complex in H_2O) was added to each slide, and
550 the sections were incubated for 5 min at RT. After that time, the Blocking buffer was
551 removed and 50 µl of Primary Antibody Solution (3x SSC Buffer, 2 % BSA, 0.1 % Triton
552 X-100, 6.4 U/µl RNase inhibitor in H_2O with GFP antibody (Aves Lab, GFP-1010)
553 diluted 1:50) was applied to each well. The sections were incubated for 30 min at RT.
554 The Primary Antibody Solution was removed, and 100 µl of Wash Buffer (3x SSC
555 Buffer, 2 % BSA, 0.1 % Triton X-100 (w/v), 1 U/µl RNase inhibitor, 10 % Ribonucleoside
556 Vanadyl Complex in H_2O) was added to each well. The Wash Buffer was directly
557 removed and the washing step was repeated for a total of five washes. Next, 50 µl of
558 Secondary Antibody Solution (3x SSC Buffer, 2 % BSA, 0.1 % Triton X-100, 6.4 U/µl
559 RNase inhibitor in H_2O with secondary antibody (diluted 1:100 and DAPI 1:220) was
560 added to each well and incubated for 30 min at RT. The Secondary Antibody Solution
561 was removed, and 100 µl of Wash Buffer was added again. The Wash Buffer was
562 removed and the washing step was repeated for a total of five washes. After removing
563 the slide from the visium slide cassette, it was immersed 20 times in 50 ml of 3x SSC

564 buffer, and 200 µl of Mounting Medium (85 % Glycerol, 2 U/µl Rnase inhibitor in H_2O)
565 was added to cover the tissue, followed by the application of a coverslip. Imaging was
566 performed immediately. Afterwards, the coverslip was removed by immersing the slide
567 in 3x SSC buffer until it slowly detached. The slide was placed back in a clean visium
568 slide cassette for the visium spatial gene expression experiment.

569 *Visium Spatial Gene Expression experiment*

570 The experiments following fluorescence staining were carried out using the "Visium
571 Spatial Gene Expression Slide & Reagent Kit" (10X Genomics) in accordance with the
572 manufacturer's protocol. In summary, the procedure involved several key steps to
573 ensure successful library preparation and gene expression analysis. Initially, tissue
574 sections were subjected to controlled permeabilization to allow access to intracellular
575 RNA. This was followed by reverse transcription. Next, second strand synthesis was
576 performed to generate double-stranded cDNA. The resulting cDNA was denatured to
577 separate the strands, and the single-stranded cDNA was subsequently amplified
578 through a series of PCR cycles. The amplified cDNA underwent a cleanup process to
579 remove reaction by-products. Following cDNA purification, the samples were subjected
580 to a step of fragmentation, end repair and A-tailing to create suitable 3' ends for adaptor
581 ligation. Adaptors were then ligated to the DNA fragments to facilitate downstream
582 sequencing. Post-ligation cleanup was performed to eliminate excess adapters.
583 Finally, a sample index PCR was carried out to introduce unique sample indices,
584 enabling the multiplexing of samples during sequencing.

585 *Immunohistochemistry imaging of sagittal brain slices*

586 Animals were anesthetized via intraperitoneal injection of 10% ketamine and 2%
587 xylazine, followed by transcardial perfusion with 1x PBS for 8 min and 4%
588 paraformaldehyde (PFA) for 20 min (flow rate 3 ml/min). Brains were dissected and

589 post-fixed in 4% PFA for 30 min at room temperature (RT) followed by incubation in
590 30% sucrose at 4°C for 2 days. To generate slices, brains were partially embedded in
591 Tissue Tek and frozen at -20 °C for 30 min. Sagittal sections (30 µm) were cut using a
592 Leica CM1950 Cryostat (chamber temperature -20 °C; block temperature -20 °C) and
593 immediately stored in 1x PBS.

594 Sagittal brain slices were washed three times with 1X PBS for 10 min and
595 blocked/permeabilized with 5% bovine serum albumin (BSA) and 0.5% Triton-X in PBS
596 for 1 h. Primary antibodies were diluted in blocking/permeabilization solution and
597 incubated over night at 4°C. After washing three times with 1X PBS for 10 min
598 secondary antibodies were diluted in blocking/permeabilization solution and incubated
599 for 2 h at RT. Slices were washed three times with 1X PBS for 10 min and incubated
600 in DAPI (dilution 1:1000 in PBS) for 10 min. For quenching slices were dried on a slide
601 and incubated in TrueBlack solution (20X TrueBlack to 1X in 70% ethanol). After
602 washing with 1X PBS, slices were mounted with Fluoromount-G. Imaging was done
603 using a confocal LSM980 microscope and formatted using Imaris 10.1.1. Astrocytes
604 were manually counted and statistical testing was performed via unpaired Student´s t-
605 test in GraphPad Prism 9.5.1.

606 *Sequencing and alignment of single nucleus samples*

607 Paired 150bp snRNA-seq was performed using the 10X Genomics Gene Expression
608 (GEX) 3´protocol with a NovaSeq 6000 sequencer. For the alignment of reads, a
609 custom reference was created by adding the sequences of the V1S/SV2 transgene
610 and the *Camk2a* promoter to the mm10 mouse reference genome. Count matrices
611 were obtained using the *cellranger count 7.1*[54] pipeline, including introns.

612 *Sequencing and alignment of Visium Spatial samples*

613 Paired 150bp snRNA-seq was performed using the NovaSeq 6000 sequencer.
614 Sequences were fiducially aligned to spots using Loupe Browser ver. 8. All aligned
615 sequences were mapped using *spaceranger count* 3.0.1 with a custom reference,
616 which included sequences for the promotor and transgene (Camk2aTTA, V1S/SV2) to
617 the mouse genome mm39.

618 *Quality Control of snRNA*

619 Count matrices generated by *cellranger count 7.1*[54] were loaded into an AnnData
620 object and processed using the Python-based framework *Scanpy 1.10.2*[55]. Integration
621 with R, where needed, was facilitated through the rpy2 package. Raw count matrices
622 were corrected for ambient RNA contamination using the *SoupX 1.6.2*[56]. To remove
623 potential doublets, *scDblFinder 1.18.0*[57] was employed with a fixed seed (123). Nuclei
624 with nUMI and nGenes values exceeding three median absolute deviations (MADs)
625 from the median were excluded. Genes detected in fewer than five nuclei across the
626 dataset were excluded. The resulting dataset was normalized via
627 *scanpy.pp.normalize_total* and *scanpy.pp.log1p*. Highly variable genes were identified
628 using the function *scanpy.pp.highly_variable_genes* with the Seurat v3 flavor, selecting
629 the top 4,000 genes. Dimensionality reduction was performed using principal
630 component analysis (PCA) and batch effects were corrected using the python-
631 implemented version of Harmony via the function
632 *scanpy.external.pp.harmony_integrate*. Harmony embeddings were then used to
633 construct a k-nearest neighbor (kNN) graph with *scanpy.pp.neighbors*. Clustering was
634 performed using Leiden clustering with standard parameters via the function
635 *scanpy.tl.leiden*.

636 *Quality Control of Visium Spatial*

637 We filtered each sample of the Visium Spatial dataset based on the MAD filtering of
638 number of reads (nUMI), number of genes (nGene), and percentage of mitochondrial
639 genes (percent.mt). A spot was filtered out if it was outside of 3x MAD value in at least
640 two metrics. Filtered samples were merged into one Seurat 5.1.0 object[25] and we
641 obtained normalized counts by the *SCTransform* function of Seurat. Integration was
642 performed using *Harmony 1.2.0*[58] on 50 PCA embeddings and clustering was done
643 using Leiden clustering based on 30 harmony embeddings. Integrated clusters were
644 visualized using the UMAP method. Samples that were not successfully integrated
645 (based on similarity measures of the harmony embeddings) and showed high
646 percentage.mt or low nUMI levels compared to other samples, were removed from
647 subsequent analysis. A final integration and clustering were performed after filtering.

648 *Annotation of Cell types in snRNA*

649 Clusters were annotated using literature, the mousebrain (mousebrain.org)[21], and
650 markers identified via the *FindConservedMarkers* function in Seurat. First, neurons and
651 non-neuronal cells were distinguished using mainly canonical markers, such as but not
652 limited to *Rbfox3* (neurons), *Mbp* (oligodendrocytes), *Acsbg1* (astrocytes), *Pdgfra*
653 (oligodendrocyte precursor cells), *Inpp5d* (microglia), *Colec12* (vascular cells), and *Ttr*
654 (choroid plexus cells). Neurons were further classified into Vglut1 (*Slc17a7*), Vglut2
655 (*Slc17a6*), GABA (*Gad2*), cholinergic (*Scube1*), and dopaminergic (*Th*) neurons.
656 Vglut1 and GABA neurons were further annotated into subtypes based on
657 subclustering and *FindConservedMarkers* markers. A full list of markers and cell types
658 can be found in the Suppl. Table 5.

659 *Annotation of Regions in Visium Spatial*

660 Regions were first annotated based on a 0.1 resolution clustering to get high level
661 region annotation (Cortex, Hippocampus, Subcortex). Each high-level region was

662 further annotated based on either more granular resolutions or subclustering. Marker
663 genes from mousebrain (mousebrain.org)[21] and literature were used in combination
664 with the Allen mouse brain atlas[19,20] to obtain anatomically relevant annotations. All
665 used markers can be seen in Suppl. Table 1.

666 *Differential Gene Expression Analysis for snRNA*

667 Counts were pseudo-bulked to sample level and filtered for counts above three in at
668 least two samples. Mitochondrial and ribosomal genes were also removed. We created
669 a *Deseq2 1.44.0* object[59,60] to normalize counts and calculate covariates using *sva*
670 *3.52.0*[61]. Sva covariates and condition were included into the design (~ SV1 +
671 condition) to perform Wald testing. P-values were recalculated using *fdrtool 1.2.18*[62]
672 with the "stat" values and adjusted p-values were obtained by Benjamini-Hochberg[63]
673 procedure as applied in the R function *p.adjust*. A gene was considered significantly
674 differentially expressed if the change was below an FDR of 0.05.

675 *Differential Gene Expression Analysis for Visium Spatial*

676 Counts were pseudo-bulked to Sample-Region. For the "Spreading Signature" we
677 compared Sample-Spreading Area to Sample-No Spreading Area. Counts were filtered
678 for counts above three in at least three samples and mitochondrial genes were
679 removed. Covariates were calculated using sva on a sample wise paired design, which
680 led to the final design: ~ SV1 + condition + condition:sample.n + condition:region. Wald
681 testing was performed, p-values were recalculated using fdrtool with the "stat" values
682 and adjusted p-values were obtained by Benjamini-Hochberg procedure as applied in
683 the R function *p.adjust*. Cell number differences between the regions were accounted
684 for by subsampling to a maximum number of cells of two-fold difference. Subsampling
685 was performed accordingly and everything was run 100 times. Only genes that were

686 below 0.05 FDR in at least 95 of 100 runs were deemed as significant. All differential
687 results can be seen in the Suppl. Table 2.

688 *Ligand-Receptor Analysis for Visium Spatial*

689 Ligand-Receptor (LR) interactions were calculated using *stlearn 0.4.12*[64] on an object
690 of raw counts. Counts were filtered by pp.*filter_genes* function with the *min_cells*
691 parameter of 3. Normalization was performed by pp.*normalize_total* function. The used
692 LR database was downloaded from stlearn via *tl.cci.load_lrs* with species set as
693 "mouse" for the "connectomeDB2020_lit" database. Spatially relevant significant LR
694 pairs were calculated by *tl.cci.run* with parameters *min_spots = 20, distance = None,*
695 and *n_pairs = 10,000* followed by *tl.cci.run_cci* with the parameters *min_spots = 3,*
696 *spot_mixtures = False, sig_spots = True,* and *n_perms = 1,000.*

697 *Transcription Factor Analysis*

698 Transcription factors were found using *decoupleR 2.10.0* architecture[22]. We used the
699 Deseq2 output for the Spreading Signature as input into the function run_ulm() with
700 the standard parameters. We used the collectTRI mouse database as *net* and set
701 minsize to 5.

702 *Inference of Networks*

703 Using PIDC, the most interconnected genes were chosen based on T. E. Chan et
704 al.[23,65]. PIDC, based on Partial Information Decomposition (PID), infers statistical
705 dependencies between triplets of genes from a single-cell gene expression matrix by
706 assigning a confidence score to each interaction. Only the genes with a top 5%
707 confidence score were used to build an interaction network using curated public
708 databases of known interactions. Central genes were defined based on the
709 betweenness centrality scores calculated via the *igraph 2.0.3*[66] architecture.

710 *Finding Interactions in interaction databases*

711 The OmniPath database[67] was accessed using *OmnipathR 3.11.16*[67] and combined
712 with interactions having a confidence score above 0.600 from full network type
713 STRING[68]. We included protein complexes and post translational modifications from
714 OmniPath as interactions. An interaction was considered "Found" in the database, if
715 the connection had a maximum of one bridge gene between the two interactors.

716 *Spot deconvolution*

717 Visium spatial spots were deconvoluted using an annotated snRNA dataset from the
718 same mouse model. We used the *CARD 1.1* package[69] to deconvolute sample wise
719 each spot for astrocyte, microglia, oligodendrocyte, OPC, vascular cells, choroid
720 plexus, cholinergic neurons, dopaminergic neuron, GABAergic neuron, Vglut1 neuron,
721 and Vglut2 neuron. The default parameters were used for creating and deconvoluting
722 CARD object with minCountGene set to 100 and minCountSpot to 5.

723 *Analysis of Cell type composition differences*

724 Cell type composition was based on the percentages from deconvoluted spots by
725 CARD. Most probable changes were calculated using *tascCODA 0.1.3*[70] by using all
726 cell types as a reference once. Changes were deemed significant if it was changed in
727 at least 66% of reference iterations with a maximum p-value of 0.2.

728 *Module Score Analysis*

729 Module score of "Spreading Signature" for snRNA dataset was obtained using the
730 Seurat function AddModuleScore. The difference of Module Scores between
731 conditions per cell type was tested for significance using the Wilcoxon-mann-Whitney
732 test[71] via the R function *wilcox.test().* We calculated the effect size for each comparison
733 using the *cliff.delta()* R function[72].

734 *Term Enrichment analysis*

735 GO and KEGG term enrichment was performed using the R packages *clusterProfiler*
736 *4.12.1*[73] and *pathfindR 2.4.1*[74] respectively. Both were run with default parameters,
737 with minGSSize for enrichGO function set to 15. Enriched KEGG terms containing one
738 of the terms "Addiction, Corona, Infection, Invasion, Cancer, Alcohol, Chagas disease,
739 Cushing, Glioma, Melano, Oocyte, Hepatitis, Tuberculosis, African, Viral, Carcinoma,
740 Circadian, Cardiomyocytes, Leukemia, Infection, cardiomyopathy" were not
741 considered for downstream analysis. For enriched GO or KEGG terms from Vglut1
742 subtypes we only considered terms relevant containing one of the terms "synapse,
743 synaptic, neurotransmitter, vesicle, transmitter, astrocyte, astrocytic, transmembrane
744 signaling, cell adhesion"

745 *Comparing with Human data*

746 We used the snRNA dataset from Smajic et al., 2022[16]. DEG analysis was performed
747 on pseudo-bulked samples with Deseq2 Wald testing for each cell type using the
748 annotation from the original publication. The astrocyte PD vs. Control results were
749 compared to our astrocyte ON vs OFF from snRNA-seq data of mice.

750

Data and code availability

The raw sequencing data that was generated in this study is available from ArrayExpress with the identifier E-MTAB-15216 for visium spatial data and the identifier E-MTAB-15158 for snRNA data. Detailed metadata, processed seurat objects, counts, spatial images and so on can be found on Zenodo with the DOI *10.5281/zenodo.15274014* for 3-months visium spatial data and the DOI *10.5281/zenodo.14988055* for 20/23-months visium and snRNA data. The code, including helper objects and functions, for analysis and figure generation is available on GitHub: https://github.com/DanzerLab/PD_VisiumSpatial_MouseBrain_Aging

Conflict of Interest

The authors declare no competing interests.

Acknowledgements

We thank R. Bück for their excellent work and technical support.

Funding Source

This work was supported and funded by the Deutsche Forschungsgemeinschaft (DFG) Emmy Noether Research Group DA 1657/2-1, GRK 1789 (CEMMA) and SFB 1506 (Aging at Interfaces).

Author Contribution

K.M. Danzer and J. LeeBae designed the project. V. Bopp, A. Goreth, J.K. Kühlwein, L. Meier, and D. Rombach performed experiments and analyzed the data. V. Bopp, A. Goreth, and J. LeeBae prepared graphs and designed figures. E. Gazzola performed quality control and annotation of cell types for snRNA-seq data. J. LeeBae performed all other bioinformatic analysis. V. Grozdanov, L. Dimou provided intellectual input. J. LeeBae and K.M. Danzer wrote the manuscript. All authors have revised or critically reviewed the article.

References

1. Lewy FH. Paralysis agitans. I. Pathologische Anatomie. In: Lewandowsky M, ed. *Handbuch der Neurologie*. Springer; 1912:920 - 958.
2. Braak H, Del Tredici K, Rub U, de Vos RA, Jansen Steur EN, Braak E. Staging of brain pathology related to sporadic Parkinson's disease. *Neurobiology of aging*. Mar-Apr 2003;24(2):197-211. doi:10.1016/s0197-4580(02)00065-9
3. Kordower JH, Chu Y, Hauser RA, Freeman TB, Olanow CW. Lewy body-like pathology in long-term embryonic nigral transplants in Parkinson's disease. *Nat Med*. May 2008;14(5):504-6. doi:10.1038/nm1747
4. Li JY, Englund E, Holton JL, et al. Lewy bodies in grafted neurons in subjects with Parkinson's disease suggest host-to-graft disease propagation. *Nat Med*. May 2008;14(5):501-3. doi:10.1038/nm1746
5. Desplats P, Lee HJ, Bae EJ, et al. Inclusion formation and neuronal cell death through neuron-to-neuron transmission of alpha-synuclein. *Proc Natl Acad Sci U S A*. Aug 4 2009;106(31):13010-5. doi:10.1073/pnas.0903691106
6. Henderson MX, Cornblath EJ, Darwich A, et al. Spread of α-synuclein pathology through the brain connectome is modulated by selective vulnerability and predicted by network analysis. *Nat Neurosci*. Aug 2019;22(8):1248-1257. doi:10.1038/s41593-019-0457-5
7. Osterberg VR, Spinelli KJ, Weston LJ, Luk KC, Woltjer RL, Unni VK. Progressive aggregation of alpha-synuclein and selective degeneration of lewy inclusion-bearing neurons in a mouse model of parkinsonism. *Cell Rep*. Mar 3 2015;10(8):1252-60. doi:10.1016/j.celrep.2015.01.060
8. Luk KC, Kehm V, Carroll J, et al. Pathological α-synuclein transmission initiates Parkinson-like neurodegeneration in nontransgenic mice. *Science*. Nov 16 2012;338(6109):949-53. doi:10.1126/science.1227157
9. Rey NL, George S, Steiner JA, et al. Spread of aggregates after olfactory bulb injection of α-synuclein fibrils is associated with early neuronal loss and is reduced long term. *Acta Neuropathol*. Jan 2018;135(1):65-83. doi:10.1007/s00401-017-1792-9
10. Devi L, Raghavendran V, Prabhu BM, Avadhani NG, Anandatheerthavarada HK. Mitochondrial import and accumulation of alpha-synuclein impair complex I in human dopaminergic neuronal cultures and Parkinson disease brain. *J Biol Chem*. Apr 4 2008;283(14):9089-100. doi:10.1074/jbc.M710012200
11. Danzer KM, Haasen D, Karow AR, et al. Different species of alpha-synuclein oligomers induce calcium influx and seeding. *The Journal of neuroscience : the official journal of the Society for Neuroscience*. Aug 22 2007;27(34):9220-32. doi:10.1523/JNEUROSCI.2617-07.2007
12. Shrivastava AN, Redeker V, Fritz N, et al. α-synuclein assemblies sequester neuronal α3-Na+/K+-ATPase and impair Na+ gradient. *Embo j*. Oct 1 2015;34(19):2408-23. doi:10.15252/embj.201591397
13. Choi I, Zhang Y, Seegobin SP, et al. Microglia clear neuron-released α-synuclein via selective autophagy and prevent neurodegeneration. *Nat Commun*. Mar 13 2020;11(1):1386. doi:10.1038/s41467-020-15119-w
14. Lee HJ, Kim C, Lee SJ. Alpha-synuclein stimulation of astrocytes: Potential role for neuroinflammation and neuroprotection. *Oxid Med Cell Longev*. Jul-Aug 2010;3(4):283-7. doi:10.4161/oxim.3.4.12809
15. Reddy K, Dieriks BV. Multiple system atrophy: α-Synuclein strains at the neuron-oligodendrocyte crossroad. *Molecular neurodegeneration*. Nov 26 2022;17(1):77. doi:10.1186/s13024-022-00579-z
16. Smajić S, Prada-Medina CA, Landoulsi Z, et al. Single-cell sequencing of human midbrain reveals glial activation and a Parkinson-specific neuronal state. *Brain : a journal of neurology*. Apr 29 2022;145(3):964-978. doi:10.1093/brain/awab446

17. Martirosyan A, Ansari R, Pestana F, et al. Unravelling cell type-specific responses to Parkinson's Disease at single cell resolution. *Molecular neurodegeneration*. Jan 20 2024;19(1):7. doi:10.1186/s13024-023-00699-0
18. Kiechle M, von Einem B, Höfs L, et al. In Vivo Protein Complementation Demonstrates Presynaptic α-Synuclein Oligomerization and Age-Dependent Accumulation of 8-16-mer Oligomer Species. *Cell Rep*. Nov 26 2019;29(9):2862-2874.e9. doi:10.1016/j.celrep.2019.10.089
19. Science AIfB. Data from: Allen Mouse Brain Atlas. 2004.
20. Science AIfB. Data from: Allen Reference Atlas - Mouse Brain. 2011.
21. Zeisel A, Hochgerner H, Lönnerberg P, et al. Molecular Architecture of the Mouse Nervous System. *Cell*. Aug 9 2018;174(4):999-1014.e22. doi:10.1016/j.cell.2018.06.021
22. Badia-i-Mompel P, Vélez Santiago J, Braunger J, et al. decoupleR: ensemble of computational methods to infer biological activities from omics data. *Bioinformatics Advances*. 2022;2(1):vbac016. doi:10.1093/bioadv/vbac016
23. Chan TE, Stumpf MP, Babtie ACJCs. Gene regulatory network inference from single-cell data using multivariate information measures. 2017;5(3):251-267. e3.
24. Saul D, Kosinsky RL, Atkinson EJ, et al. A new gene set identifies senescent cells and predicts senescence-associated pathways across tissues. *Nature Communications*. 2022/08/16 2022;13(1):4827. doi:10.1038/s41467-022-32552-1
25. Hao Y, Stuart T, Kowalski MH, et al. Dictionary learning for integrative, multimodal and scalable single-cell analysis. *Nature Biotechnology*. 2024/02/01 2024;42(2):293-304. doi:10.1038/s41587-023-01767-y
26. Purgert CA, Izumi Y, Jong YJ, Kumar V, Zorumski CF, O'Malley KL. Intracellular mGluR5 can mediate synaptic plasticity in the hippocampus. *J Neurosci*. Mar 26 2014;34(13):4589-98. doi:10.1523/jneurosci.3451-13.2014
27. Abe T, Sugihara H, Nawa H, Shigemoto R, Mizuno N, Nakanishi S. Molecular characterization of a novel metabotropic glutamate receptor mGluR5 coupled to inositol phosphate/Ca2+ signal transduction. *J Biol Chem*. Jul 5 1992;267(19):13361-8.
28. Uematsu K, Heiman M, Zelenina M, et al. Protein kinase A directly phosphorylates metabotropic glutamate receptor 5 to modulate its function. *J Neurochem*. Mar 2015;132(6):677-86. doi:10.1111/jnc.13038
29. Hua J, Yin N, Xu S, et al. Enhancing the Astrocytic Clearance of Extracellular α-Synuclein Aggregates by Ginkgolides Attenuates Neural Cell Injury. *Cell Mol Neurobiol*. Oct 2019;39(7):1017-1028. doi:10.1007/s10571-019-00696-2
30. Morales I, Sanchez A, Rodriguez-Sabate C, Rodriguez M. Striatal astrocytes engulf dopaminergic debris in Parkinson's disease: A study in an animal model. *PLoS One*. 2017;12(10):e0185989. doi:10.1371/journal.pone.0185989
31. Sonninen TM, Hämäläinen RH, Koskuvi M, et al. Metabolic alterations in Parkinson's disease astrocytes. *Sci Rep*. Sep 2 2020;10(1):14474. doi:10.1038/s41598-020-71329-8
32. Loria F, Vargas JY, Bousset L, et al. α-Synuclein transfer between neurons and astrocytes indicates that astrocytes play a role in degradation rather than in spreading. *Acta Neuropathol*. Nov 2017;134(5):789-808. doi:10.1007/s00401-017-1746-2
33. Tsunemi T, Ishiguro Y, Yoroisaka A, et al. Astrocytes Protect Human Dopaminergic Neurons from α-Synuclein Accumulation and Propagation. *J Neurosci*. Nov 4 2020;40(45):8618-8628. doi:10.1523/jneurosci.0954-20.2020
34. Rostami J, Holmqvist S, Lindström V, et al. Human Astrocytes Transfer Aggregated Alpha-Synuclein via Tunneling Nanotubes. *J Neurosci*. Dec 6 2017;37(49):11835-11853. doi:10.1523/jneurosci.0983-17.2017
35. Braak H, Sastre M, Del Tredici K. Development of alpha-synuclein immunoreactive astrocytes in the forebrain parallels stages of intraneuronal pathology in sporadic Parkinson's disease. *Acta Neuropathol*. Sep 2007;114(3):231-41. doi:10.1007/s00401-007-0244-3

36. Sheng L, Stewart T, Yang D, et al. Erythrocytic α-synuclein contained in microvesicles regulates astrocytic glutamate homeostasis: a new perspective on Parkinson's disease pathogenesis. *Acta Neuropathol Commun*. Jul 8 2020;8(1):102. doi:10.1186/s40478-020-00983-w
37. Banerjee R, Raj A, Potdar C, et al. Astrocytes Differentiated from LRRK2-I1371V Parkinson's-Disease-Induced Pluripotent Stem Cells Exhibit Similar Yield but Cell-Intrinsic Dysfunction in Glutamate Uptake and Metabolism, ATP Generation, and Nrf2-Mediated Glutathione Machinery. *Cells*. Jun 8 2023;12(12)doi:10.3390/cells12121592
38. Trudler D, Sanz-Blasco S, Eisele YS, et al. α-Synuclein Oligomers Induce Glutamate Release from Astrocytes and Excessive Extrasynaptic NMDAR Activity in Neurons, Thus Contributing to Synapse Loss. *J Neurosci*. Mar 10 2021;41(10):2264-2273. doi:10.1523/jneurosci.1871-20.2020
39. Aronica E, Gorter JA, Ijlst-Keizers H, et al. Expression and functional role of mGluR3 and mGluR5 in human astrocytes and glioma cells: opposite regulation of glutamate transporter proteins. *Eur J Neurosci*. May 2003;17(10):2106-18. doi:10.1046/j.1460-9568.2003.02657.x
40. Ossowska K, Konieczny J, Wardas J, et al. An influence of ligands of metabotropic glutamate receptor subtypes on parkinsonian-like symptoms and the striatopallidal pathway in rats. *Amino Acids*. Feb 2007;32(2):179-88. doi:10.1007/s00726-006-0317-y
41. Phillips JM, Lam HA, Ackerson LC, Maidment NT. Blockade of mGluR glutamate receptors in the subthalamic nucleus ameliorates motor asymmetry in an animal model of Parkinson's disease. *Eur J Neurosci*. Jan 2006;23(1):151-60. doi:10.1111/j.1460-9568.2005.04550.x
42. Cuomo D, Martella G, Barabino E, et al. Metabotropic glutamate receptor subtype 4 selectively modulates both glutamate and GABA transmission in the striatum: implications for Parkinson's disease treatment. *J Neurochem*. May 2009;109(4):1096-105. doi:10.1111/j.1471-4159.2009.06036.x
43. Masilamoni GJ, Bogenpohl JW, Alagille D, et al. Metabotropic glutamate receptor 5 antagonist protects dopaminergic and noradrenergic neurons from degeneration in MPTP-treated monkeys. *Brain : a journal of neurology*. Jul 2011;134(Pt 7):2057-73. doi:10.1093/brain/awr137
44. Battaglia G, Busceti CL, Molinaro G, et al. Endogenous activation of mGlu5 metabotropic glutamate receptors contributes to the development of nigro-striatal damage induced by 1-methyl-4-phenyl-1,2,3,6-tetrahydropyridine in mice. *J Neurosci*. Jan 28 2004;24(4):828-35. doi:10.1523/jneurosci.3831-03.2004
45. Südhof TC. The cell biology of synapse formation. *J Cell Biol*. Jul 5 2021;220(7)doi:10.1083/jcb.202103052
46. Di Micco R, Krizhanovsky V, Baker D, d'Adda di Fagagna F. Cellular senescence in ageing: from mechanisms to therapeutic opportunities. *Nature Reviews Molecular Cell Biology*. 2021/02/01 2021;22(2):75-95. doi:10.1038/s41580-020-00314-w
47. Ma Y, Erb ML, Moore DJ. Aging, cellular senescence and Parkinson's disease. *Journal of Parkinson's Disease*. 2025/03/01 2025;15(2):239-254. doi:10.1177/1877718X251316552
48. Chinta SJ, Woods G, Demaria M, et al. Cellular Senescence Is Induced by the Environmental Neurotoxin Paraquat and Contributes to Neuropathology Linked to Parkinson's Disease. *Cell Rep*. Jan 23 2018;22(4):930-940. doi:10.1016/j.celrep.2017.12.092
49. Lee SJ, Lim HS, Masliah E, Lee HJ. Protein aggregate spreading in neurodegenerative diseases: problems and perspectives. *Neurosci Res*. Aug 2011;70(4):339-48. doi:10.1016/j.neures.2011.05.008
50. Clarke LE, Liddelow SA, Chakraborty C, Münch AE, Heiman M, Barres BA. Normal aging induces A1-like astrocyte reactivity. *Proc Natl Acad Sci U S A*. 2018/02// 2018;115(8):E1896-E1905. doi:10.1073/pnas.1800165115
51. Ishii T, Takanashi Y, Sugita K, et al. Endogenous reactive oxygen species cause astrocyte defects and neuronal dysfunctions in the hippocampus: a new model for aging brain. *Aging Cell*. Feb 2017;16(1):39-51. doi:10.1111/acel.12523
52. Ferrer I. Diversity of astroglial responses across human neurodegenerative disorders and brain aging. *Brain Pathol*. Sep 2017;27(5):645-674. doi:10.1111/bpa.12538

53. Mayford M, Bach ME, Huang YY, Wang L, Hawkins RD, Kandel ER. Control of memory formation through regulated expression of a CaMKII transgene. *Science*. Dec 6 1996;274(5293):1678-83. doi:10.1126/science.274.5293.1678

54. Zheng GX, Terry JM, Belgrader P, et al. Massively parallel digital transcriptional profiling of single cells. *Nat Commun*. Jan 16 2017;8:14049. doi:10.1038/ncomms14049

55. Wolf FA, Angerer P, Theis FJ. SCANPY: large-scale single-cell gene expression data analysis. *Genome Biol*. Feb 6 2018;19(1):15. doi:10.1186/s13059-017-1382-0

56. Young MD, Behjati S. SoupX removes ambient RNA contamination from droplet-based single-cell RNA sequencing data. *Gigascience*. Dec 26 2020;9(12)doi:10.1093/gigascience/giaa151

57. Germain PL, Lun A, Garcia Meixide C, Macnair W, Robinson MD. Doublet identification in single-cell sequencing data using scDblFinder. *F1000Res*. 2021;10doi:10.12688/f1000research.73600.2

58. Korsunsky I, Millard N, Fan J, et al. Fast, sensitive and accurate integration of single-cell data with Harmony. *Nature Methods*. 2019/12/01 2019;16(12):1289-1296. doi:10.1038/s41592-019-0619-0

59. Love MI, Huber W, Anders S. Moderated estimation of fold change and dispersion for RNA-seq data with DESeq2. *Genome Biology*. 2014/12/05 2014;15(12):550. doi:10.1186/s13059-014-0550-8

60. Love M, Anders S, Huber WJGB. Differential analysis of count data–the DESeq2 package. 2014;15(550):10-1186.

61. Leek JT. svaseq: removing batch effects and other unwanted noise from sequencing data. *Nucleic Acids Res*. Dec 1 2014;42(21):e161. doi:10.1093/nar/gku864

62. Strimmer K. fdrtool: a versatile R package for estimating local and tail area-based false discovery rates. *Bioinformatics*. 2008;24(12):1461-1462. doi:10.1093/bioinformatics/btn209

63. Benjamini Y, Hochberg Y. Controlling the False Discovery Rate: A Practical and Powerful Approach to Multiple Testing. *Journal of the Royal Statistical Society: Series B (Methodological)*. 1995;57(1):289-300. doi:10.1111/j.2517-6161.1995.tb02031.x

64. Pham D, Tan X, Balderson B, et al. Robust mapping of spatiotemporal trajectories and cell–cell interactions in healthy and diseased tissues. *Nature Communications*. 2023/11/25 2023;14(1):7739. doi:10.1038/s41467-023-43120-6

65. Chan TE, Stumpf MPH, Babtie AC. Gene Regulatory Network Inference from Single-Cell Data Using Multivariate Information Measures. *Cell Syst*. Sep 27 2017;5(3):251-267.e3. doi:10.1016/j.cels.2017.08.014

66. Nepusz GCaT. The igraph software package for complex network research. *InterJournal*. 2006;Complex Systems:1695. doi:https://igraph.org

67. Türei D, Valdeolivas A, Gul L, et al. Integrated intra- and intercellular signaling knowledge for multicellular omics analysis. *Mol Syst Biol*. Mar 2021;17(3):e9923. doi:10.15252/msb.20209923

68. Szklarczyk D, Kirsch R, Koutrouli M, et al. The STRING database in 2023: protein-protein association networks and functional enrichment analyses for any sequenced genome of interest. *Nucleic Acids Res*. Jan 6 2023;51(D1):D638-d646. doi:10.1093/nar/gkac1000

69. Ma Y, Zhou X. Spatially informed cell-type deconvolution for spatial transcriptomics. *Nature Biotechnology*. 2022/09/01 2022;40(9):1349-1359. doi:10.1038/s41587-022-01273-7

70. Ostner J, Carcy S, Müller CL. tascCODA: Bayesian Tree-Aggregated Analysis of Compositional Amplicon and Single-Cell Data. *Front Genet*. 2021;12:766405. doi:10.3389/fgene.2021.766405

71. Mann HB, Whitney DR. On a Test of Whether one of Two Random Variables is Stochastically Larger than the Other. *The Annals of Mathematical Statistics*. 3/1 1947;18(1):50-60. doi:10.1214/aoms/1177730491

72. *Effsize - a package for efficient effect size computation*. 2016.

73. Wu T, Hu E, Xu S, et al. clusterProfiler 4.0: A universal enrichment tool for interpreting omics data. *The Innovation*. 2021;2(3)doi:10.1016/j.xinn.2021.100141

74. Ulgen E, Ozisik O, Sezerman OU. pathfindR: An R Package for Comprehensive Identification of Enriched Pathways in Omics Data Through Active Subnetworks. Methods. *Frontiers in Genetics*. 2019;Volume 10 - 2019